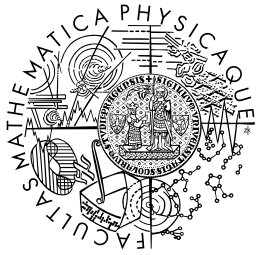

FACULTY
OF MATHEMATICS
AND PHYSICS
Charles University

BACHELOR THESIS

Tadeáš Wilczek

Study of the Belle II vertex detector resolution

Institute of Particle and Nuclear Physics

Supervisor of the bachelor thesis: prof. RNDr. Zdeněk Doležal, Dr.
Study programme: Physics
Study branch: Physics

Prague 2022

I declare that I carried out this bachelor thesis independently, and only with the cited sources, literature and other professional sources. It has not been used to obtain another or the same degree.

I understand that my work relates to the rights and obligations under the Act No. 121/2000 Sb., the Copyright Act, as amended, in particular the fact that the Charles University has the right to conclude a license agreement on the use of this work as a school work pursuant to Section 60 subsection 1 of the Copyright Act.

In ..... date ....

Author's signature

First, I would like to thank my supervisor prof. RNDr. Zdeněk Doležal, Dr. for giving me the opportunity to work on this project and learn about the Belle II experiment. I would also like to thank my consultant Mgr. Tadeáš Bilka for being patient with me and always being ready to help in case I got stuck or did not understand something.

And last but not least I would like to thank my family for always supporting me during my studies, especially near the end as I was struggling to finish all requirements on time.

Title: Study of the Belle II vertex detector resolution

Author: Tadeáš Wilczek

ústav: Institute of Particle and Nuclear Physics

Supervisor: prof. RNDr. Zdeněk Doležal, Dr., Institute of Particle and Nuclear Physics

Abstract: This bachelor thesis studies the resolution of the Belle II detector using muons from cosmic ray tracks penetrating the detector. The first part describes the Belle II experiment. The next part explains the method used to find the resolution and applies it to data from Monte Carlo simulation. Then the same method is applied on data from Spring 2020 and compared with the results acquired from analyzing the Monte Carlo simulation. The last part examines more recent data taken from 29.10.2021 to 30.3.2022. Additionally as a part of this thesis a Python script capable of providing all the results shown in this paper was developed.

Keywords: vertex detector, alignment, flavour physics

Contents

Introduction

Particle physics is a branch of physics that studies the building blocks of the Universe - particles. This includes both particles previously thought to be elementary like the proton, neutron and many more, but also more recently discovered particles. Particles are grouped into fermions (quarks, leptons) and bosons. The current theory unifying all of these particles and their interactions is called The Standard Model (Fig.1).

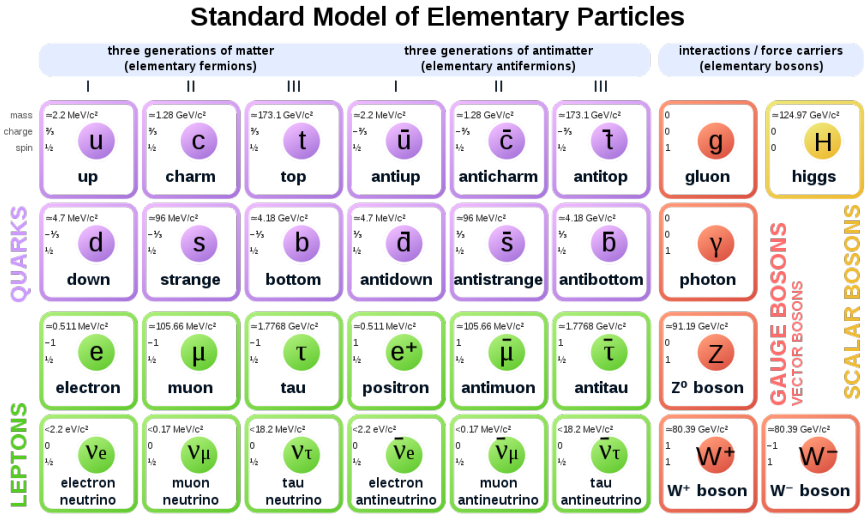

Figure 1: The Standard Model of Elementary Particles [1]

The Standard Model has been extremely beneficial to physics and led to deeper understanding of our universe, however, since its conception we have observed several phenomena that the Standard Model fails to explain. One such example is the strong CP problem. According to our current models the charge-parity symmetry can be violated both for weak and strong interactions. As of yet we have only observed CP asymmetry in weak interactions. There is hope that with a better understanding of the CP symmetry violation we could explain the matter-antimatter imbalance we see in the Universe. After the Big Bang most of matter and antimatter annihilated into the cosmic background radiation we see today, however the process was not completely symmetrical and the matter 'won'. There are multiple possible explanations of this, but the CP asymmetry is currently the best candidate to explain what we see. The effort to study phenomena not explained by the Standard Model is sometimes called exploring the physics beyond the Standard Model or New Physics.

The Belle detector was used to study the CP asymmetry in B-meson decays. It was located at the KEKB accelerator, that uses asymmetric-energy collisions of electrons and positrons. Due to its high luminosity the experiment was also used to study rare decays and search for new particles. The experiment ran from 1999 to 2010. [2]

1. The Belle II experiment

Belle II detector is an upgrade to the Belle detector. Just as Belle, Belle II is designed to study the CP asymmetry in B-meson decays. The particle accelerator was also upgraded and is now called SuperKEKB. It is designed for luminosity of 8×10^{35} $\mathrm{cm}^{-2}\mathrm{s}^{-1}$ which is about 40 times higher than the peak recorded at KEKB and 80 times its design luminosity [3]. SuperKEKB is designed to collide electrons and positrons at energies in the regions of the Υ resonances, $\Upsilon(4S)$ resonance will be used the most. The beam energies are 4 GeV for low-energy ring (LER) and 7 GeV for high-energy ring (HER)[4]. The first data was taken with Belle II in 2018, but the accelerator is not running at full capacity as of yet. It is located at KEK in Tsukuba, Ibaraki Prefecture, Japan. In the Fig. 1.1 we can see an illustration of the SuperKEKB accelerator (left) and the Belle II detector compared to a human for a sense of its scale (right).

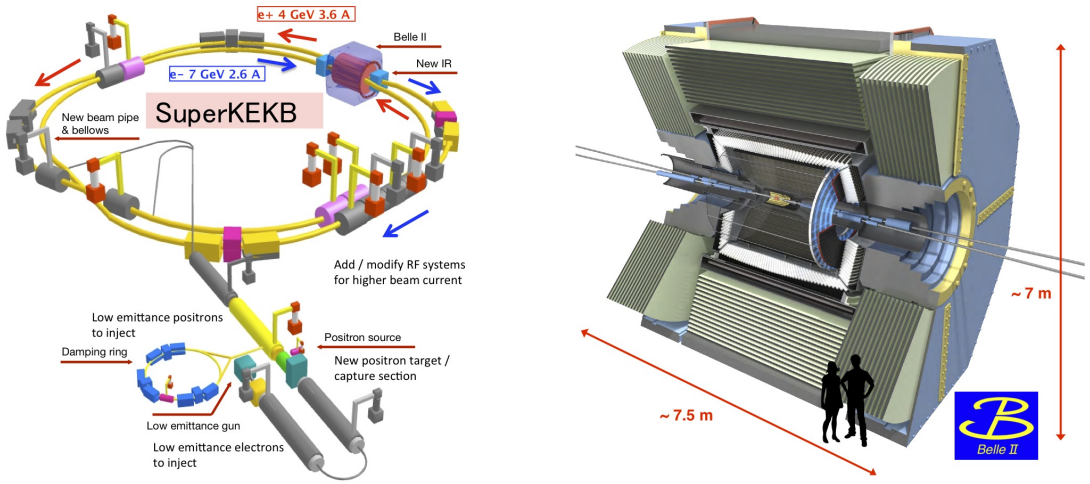

Figure 1.1: Illustration of the SuperKEKB accelerator and Belle II detector. [5]

Belle II aims to address many questions. We will not explain them fully, but they deserve to be at least mentioned. Some of them are:

- "Are there new CP violating phases in the quark sector?
- Does nature have Multiple Higgs bosons?
- Does nature have a left-right symmetry, and are there flavour-changing neutral currents beyond the SM?
- Are there sources of lepton flavour violation beyond the SM?
- Is there a dark sector of particle physics at the same mass scale as ordinary matter?
- What is the nature of the strong force in binding hadrons?"[3]

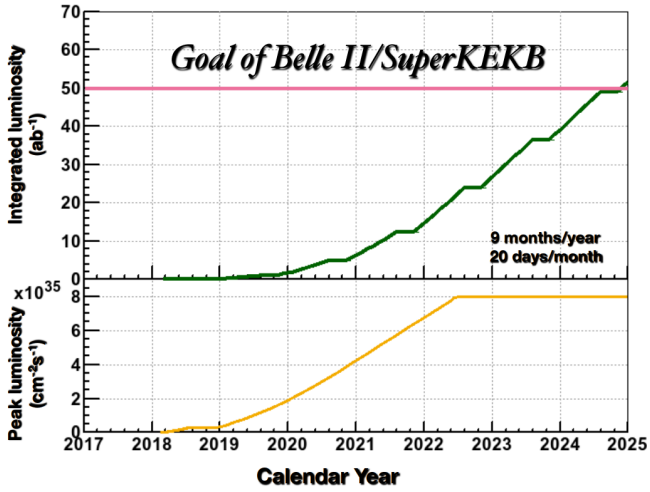

Figure 1.2: The projected peak instantaneous and integrated luminosities at SuperKEKB. [3]

As was stated earlier the SuperKEKB accelerator is not running at maximum designed luminosity as of yet. The projected peak instantaneous and integrated luminosities are (assuming nine months operation per year) shown in Fig. 1.2

The detector itself consists of multiple subdetectors, each with a different main purpose. Together they provide a complete information about the particles passing through the detector. All the parts are briefly described in the following text.

1.1 Vertex Detector (VXD)

The vertex detector (VXD) consists of two parts, the silicon Pixel Detector (PXD) and Silicon Vertex Detector (SVD). The innermost two layers of the detector consists of pixel sensors. After the initial two layers of pixels, four layers of strip sensors follow. The detectors are located in a cylinder around a 10 mm radius Be beam pipe. The schematic layout of the vertex detector can be seen in Fig. 1.3.

The beam pipe and the first two detector layers are closer to the interaction point than in Belle and the outermost layer is further.

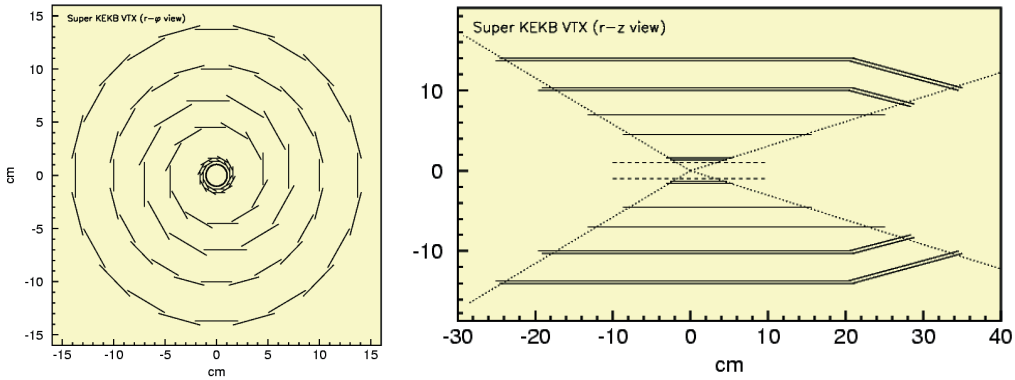

Figure 1.3: A schematic view of the Belle II vertex detector. [3]

Both parts of VXD (PXD and SVD) are silicon semiconductor detectors. When a charged particle or photon passes through the silicon it deposits energy, creating electron-hole pairs. They allow for a current to pass through the silicon. This current can be measured and used as a signal from the detector.

1.1.1 Pixel Detector (PXD)

The detectors closest to the beampipe are, at the high luminosities that Belle II is designed for, subjected to extremely high hit rates as a result of beam-related background. Due to the large occupancy the innermost layers of the detector cannot be strip detectors. Pixel detectors can solve this issue, as they have much higher number of channels and thus much smaller occupancy. Pixel detectors, as their name suggests, consist of a large number of small segments called pixels.

At the Large Hadron Collider (LHC) similar scheme was used (pixel detectors followed by strips), however at Belle II the collisions occur at much smaller energies. The silicon detectors used at LHC are too thick. The effects of multiple scattering at energies used by Belle II would make precise measurement impossible. Therefore a new pixel detector concept is used. They are called DEPFET (DEPleted Field Effect Transistor) type detectors.

The DEPFET is a semiconductor detector concept combining detection and amplification within one device. It allows the readout electronics, which need active cooling, to be located outside the acceptance region. The sensors themselves consume very little power, so air cooling is sufficient. Thus there can be much less material in the path of the particles produced in collisions. This can help reduce the multiple scattering effect, which is a bigger concern at Belle II than at LHC, since the energies are lower. The Belle II PXD is one of the most advanced pixel detectors ever developed for particle physics experiment.[4]

1.1.2 Silicon Vertex Detector (SVD)

The beam-related background increases roughly with the inverse square of the radius, therefore beyond the radii 40 mm it is safe to use strip detectors at SuperKEKB luminosities[4]. This means that after the first two layers of pixel detectors the strip detectors are used. They are similar to pixel detectors but they are composed of long strips instead of pixels. The silicon strip sensors are preferred because they avoid the huge channel count of pixels without compromising the detection capability. The design used consists of double sided silicon strip detectors (DSSDs) fabricated from six inch wafers.

SVD covers the full Belle II angular acceptance of $17° < \theta < 150°$. This range is asymmetric to accommodate for the asymmetric energies at Belle II. To avoid significantly increasing the number of wafers necessary for such coverage slanted sensors are used, as can be seen in the right part in Fig. 1.3.[4]

1.2 Central Drift Chamber (CDC)

The central drift chamber serves as a central tracking device. It is a large volume drift chamber with small drift cells. An ionizing particle passing through the chamber filled with gas ionizes the atoms of the gas, creating electrons and ions.

They are then accelerated by an electric field inside the chamber and cause charge avalanche. Their charge is then collected on a nearest wire and detected as a signal. Much like the vertex detector it extends to a larger radius than in Belle. It also has smaller drift cells, allowing for operation at higher event rates. The CDC reconstructs tracks of charged particles and measures their momenta precisely. It also allows for particle identification by measuring the energy loss within its gas volume.

The Belle CDC performed well for more than ten years, therefore Belle II CDC follows the same structure of the major parts. The main changes are to the readout electronics to handle higher trigger rates and increased volume as there is more space between the new SVD and particle identification system. The new CDC also generates three-dimensional trigger information. A z trigger for charged particles allows for reduction of background without the loss of physics events.[4]

1.3 Particle Identification System (PID)

For the purpose of identifying particles a time-of-propagation (TOP) counter is used. The TOP counter is located in the barrel. It is a special kind of Cherenkov detector. It measures a two dimensional information of a Cherenkov ring image. This is achieved by measuring both the time of arrival and impact position of Cherenkov photons. One of the modules of TOP counter can be seen in the Fig. 1.4 (left).[4]

Cherenkov radiation is produced when a charged particle passes through a dielectric material faster than the speed of light in said material. The radiation spreads at an angle to the direction of the movement of the particle. This angle is determined by the speed of the particle and the surrounding material.

In the forward end-cap region a proximity focusing Cherenkov ring imaging detector with aerogel ARICH is used as a Cherenkov radiator to identify charged particles. In Fig. 1.4 (right) an schematic representation of an element of ARICH can be seen.

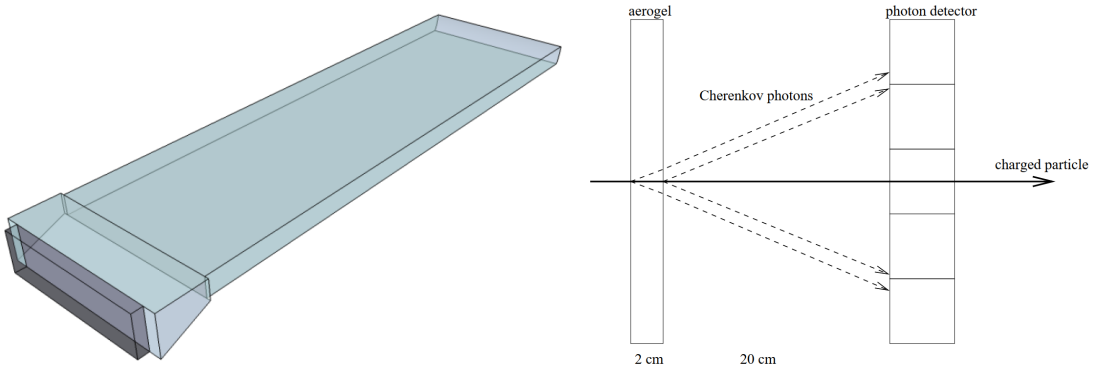

Figure 1.4: One module of the TOP counter (left) [3] and proximity focusing ARICH - principle (right) [4]

1.4 Electromagnetic Calorimeter (ECL)

The main purpose of the electromagnetic calorimeter is to measure the energy of the particles that stop inside it, mostly electrons and photons. The calorimeter consists of three regions: the barrel, forward and backward end-caps. It covers about 90% of the solid angle in the centre-of-mass system[3]. The exact layout of the electromagnetic calorimeter can be seen in Fig. 1.5.

Electromagnetic calorimeter is designed to detect particles that interact via electromagnetic interaction. When such particle enters the calorimeter it initiates a particle shower. The shower is a cascade of secondary particles produced in interactions with matter, the new particles interact in the same way again. This process stops when the produced particles no longer have enough energy to create more, they are then stopped and their energy absorbed by the calorimeter.

1.5 K_L^0 and Muon Detector (KLM)

This is the outermost part of the Belle II detector, it consists of alternating plates of iron and active detector elements. It is located outside of the solenoid. Its layout can be seen in Fig. 1.5.

The particles passing through the KLM interact with the iron atoms initiating a hadron shower. Unlike ECL the energy of the passing particles is not fully absorbed and the particles 'escape'. However it is possible to measure the positions of the individual interactions and reconstruct the trajectory of the particles.

1.6 Alignment

In order to reach the design performance of the detector, the so called calibration constants must be determined. For example for the VXD these constants describe the position, orientation and surface deformation of the individual detector segments. The process of finding the calibration constants is called alignment. For Belle II approach determining all the constants simultaneously was chosen. This was achieved using the Millepede II tool. The CDC is also integrated into this process and some constants are determined together with the VXD alignment. [3]

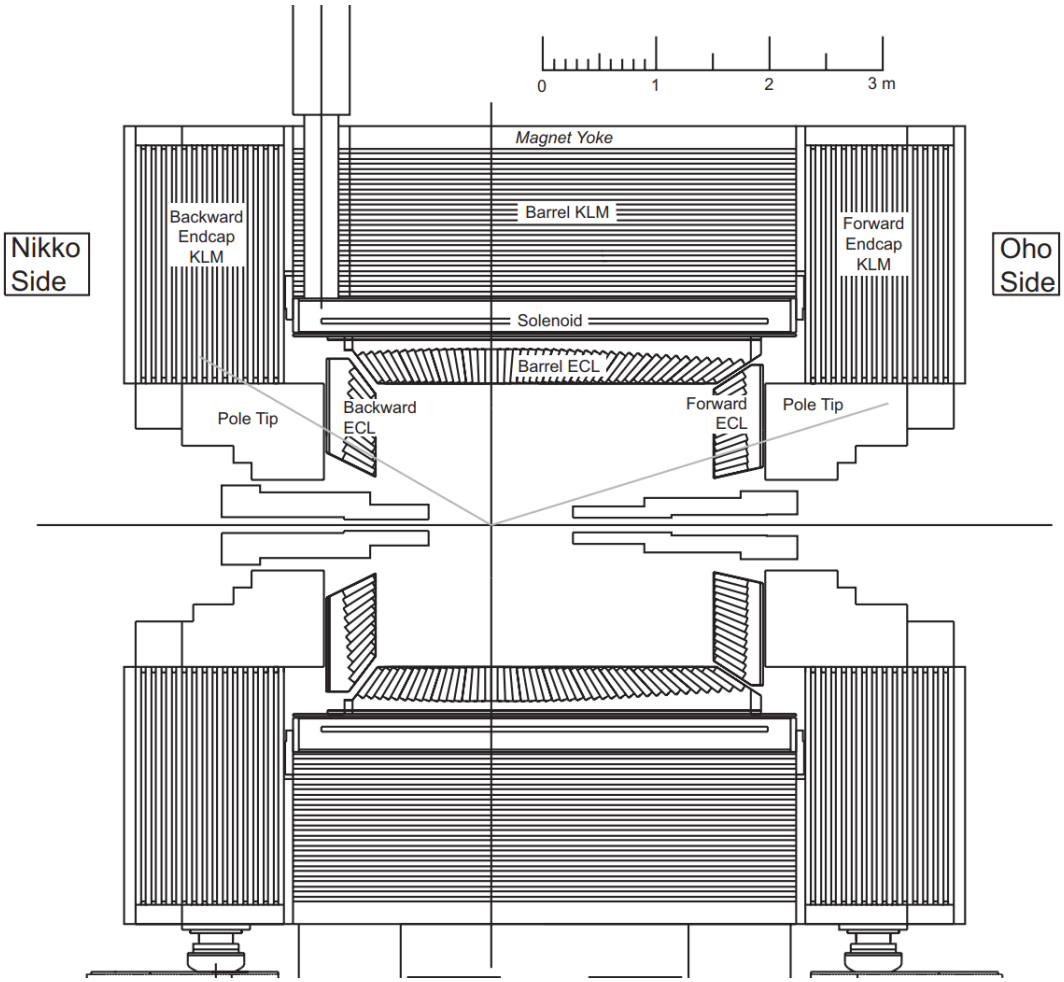

Figure 1.5: Side view of the KLM and the ECL. The gray lines mark the nominal polar angular acceptance of Belle II. [4]

2. The Analysis Method

We will find the resolution of the Belle II detector using cosmic radiation. After passing through the Earth's atmosphere the cosmic radiation consists mostly of muons. Some of these muons reach the detector underground. We can separate the tracks detected by the detector into upper and lower parts at the closest point of approach to the origin. We reconstruct these tracks separately and compare them. This will be the basis of our method and allows us to check the quality of the alignment and the final resolution of the detector.

Muons from cosmic rays can have much higher momenta than particles produced in collisions. Particles with higher momenta are less affected by multiple scattering effects. This allows us to find the resolution of the detector itself in an infinite momenta limit.

2.1 Monte Carlo Simulation

First we will apply this method to an ideal scenario - data provided by the Monte Carlo simulation. The simulation was first made for the Belle detector and later modified to fit the Belle II detector. Outside of the detector the simulation is not as precise to save computation time and it may be slightly different from real data. However, the difference is only small and affects only which particles actually reach the detector and not what happens inside. The differences will be discussed in more detail later. The data from the Monte Carlo simulation will be denoted as MC.

We will describe the tracks with helix parameters. We are essentially using cylindrical coordinate system when describing the tracks, z_0 is the position of the closest point of approach to the origin of the track on the z axis, d_0 is the distance of this point from the z axis, ϕ_0 is the angle of the tracks in a plane perpendicular to the z axis, λ is the angle between the track his plane and P_t is the transverse momentum. The helix parameters are shown for an example track in Fig. 2.1

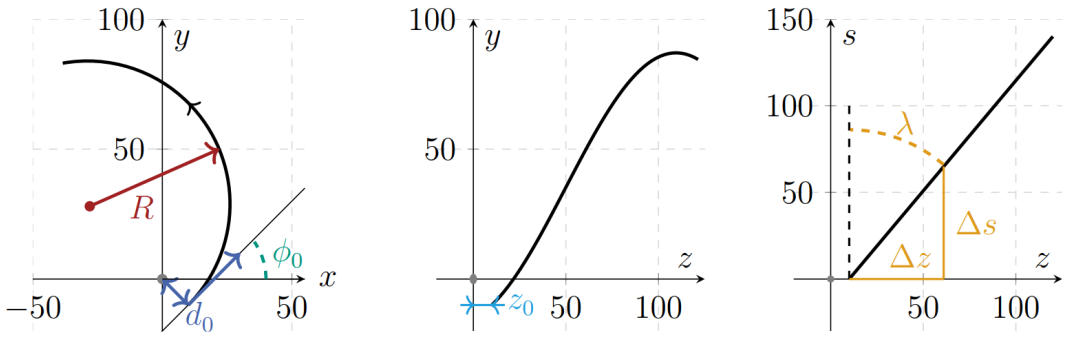

Figure 2.1: Helix parameters for a schematic representation of a track's trajectory in the $x-y$ (left), $z-y$ (middle) and $z-s$ (right) projections. All dimensions are in cm. s is the path length along the circular trajectory in the $x-y$ projection and R is the track radius. [6]

Helix parameters in general will be denoted as h. h_1 describes the upper track

and h_2 the lower. The difference of these tracks is calculated as

$$\Delta h = \frac{h_1 - h_2}{\sqrt{2}}. \tag{2.1}$$

Sometimes we will use the average of the tracks instead of their individual values, as it makes the plots easier to read, especially if we plot multiple data sets. The averages are calculated as

$$\overline{h} = \frac{h_1 + h_2}{2} \tag{2.2}$$

We will use only full cosmic tracks, which cross all three tracking subdetectors: PXD, SVD and CDC [7]. We require at least one PXD hit and at least four VXD hits on each arm. We will use only the data from cosmic events by choosing only events with $|z_0| > 0.3$ cm. This eliminates the events from collisions, as they are usually close to the origin. For MC we are left with 132098 events. The histograms of $\overline{h}$ of these events are in Figs. 2.2 to 2.7.

In Fig. 2.5 we can clearly see the restriction $|z_0| > 0.3$ cm. In Fig. 2.3 we can see that most of the muons reach the detector in the vertical direction and horizontal tracks are rare. This makes sense as in the second case muons have to pass through more matter to reach the detector. This is a significant difference in the data from cosmic events to the data from collisions. However, since the detector is symmetrical around the z axis, our results can be used even for the tracks from collisions as there is no real difference between the tracks in the horizontal and vertical directions.

2.2 Resolutions for a Range of Momenta

As we said earlier, the particles with higher momenta are less affected by multiple scattering. We chose the range of 4 GeV/c to 5 GeV/c, as it still contains a good portion of events as can be seen in Fig. 2.7. In Fig. 2.8 we can see that the resolution is affected very little by multiple scattering for pseudomomentum higher than 4 GeV/c. While we are not choosing the events based on pseudomomentum but P_t, it is a good first estimate as can be seen in Figs. A.1 and A.2. These figures can be found in appendix A.1 and were drawn using the same method as the plots in Sect. 2.4, except the errors were estimated as $\frac{\sigma}{\sqrt{N}}$ where σ is the standard deviation. Only events with 4 GeV/c $< P_t <$ 5 GeV/c were plotted. From these figures we can see that the resolution stays mostly constant and that the pseudomomentum of most events is close to P_t. When we choose 4 GeV/c $< P_t <$ 5 GeV/c we are essentially neglecting the geometry of the tracks. But as can be seen from Figs. 2.3 and 2.6, most of our tracks are in the vertical direction and we can expect for most events $\theta > 45°$ ($\theta = 90° - \lambda$).

After restricting the momentum, we are left with 11752 events for MC. We plotted the histograms of Δh, showing 96% of events (range between 2-nd and 98-th percentile). The same range was fitted with a normal distribution multiplied by a constant a

$$y = \frac{a}{\sigma\sqrt{2\pi}} e^{-\frac{1}{2}\left(\frac{x-\mu}{\sigma}\right)^2} \tag{2.3}$$

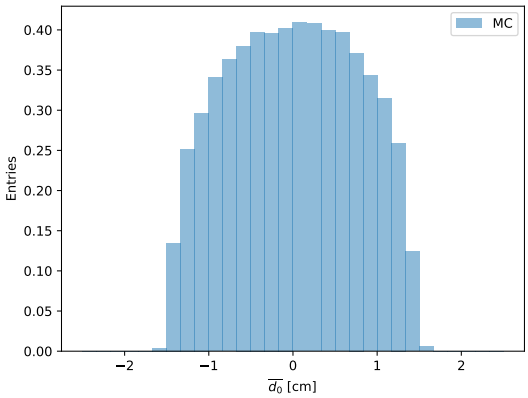

Figure 2.2: Histogram of $\overline{d_0}$ for MC

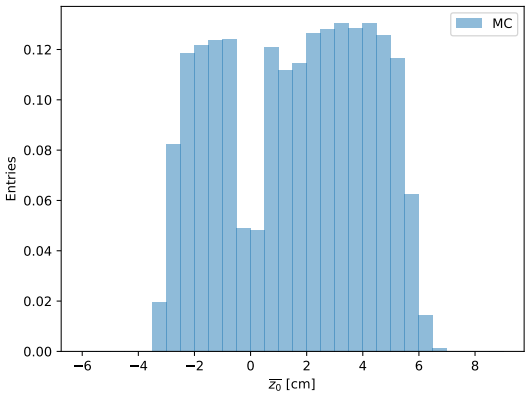

Figure 2.5: Histogram of $\overline{z_0}$ for MC

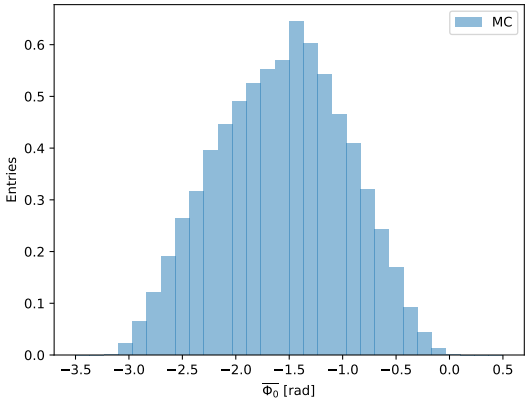

Figure 2.3: Histogram of $\overline{\phi_0}$ for MC

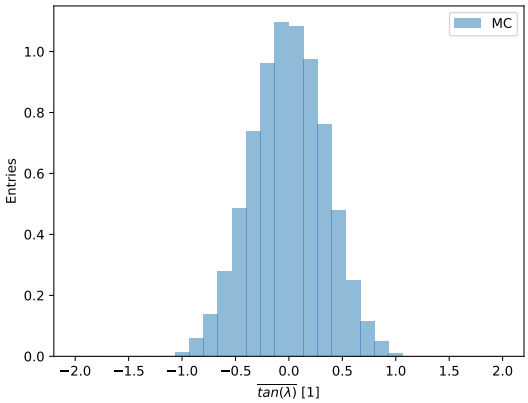

Figure 2.6: Histogram of $\overline{\tan(\lambda)}$ for MC

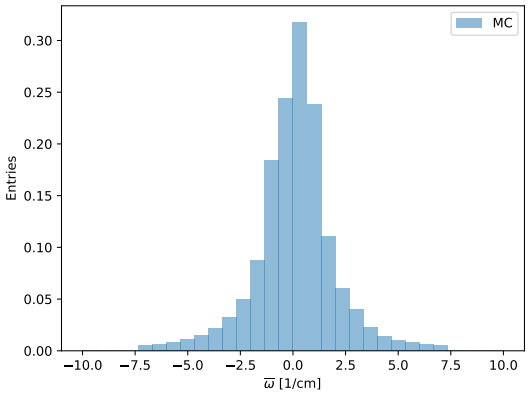

Figure 2.4: Histogram of $\overline{\omega}$ for MC

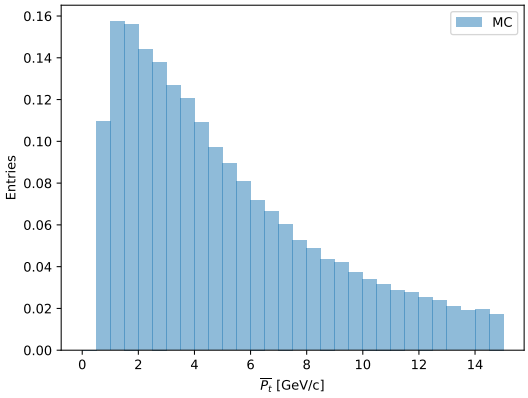

Figure 2.7: Histogram of $\overline{P_t}$ for MC

using the least squares method. The fit parameters a, μ and σ are written above each histogram. Additionally for the sake of clarity they are written in Table 3.1, which is located in Sect. 3.2 for easier comparison with other data. The histograms can be seen in Fig. 2.9

In Fig. 2.9 the fit using 2.3 seems to describe the simulated data well, but for $\Delta\phi$ and $\Delta \tan\lambda$ we can observe slight inaccuracies near the edges. But if we plot all the events (all P_t) in Fig. A.3, we start to see that the distribution is not normal. However, since the Gaussian fits the MC well enough, in Fig. 2.9, we will use it to estimate μ and σ.

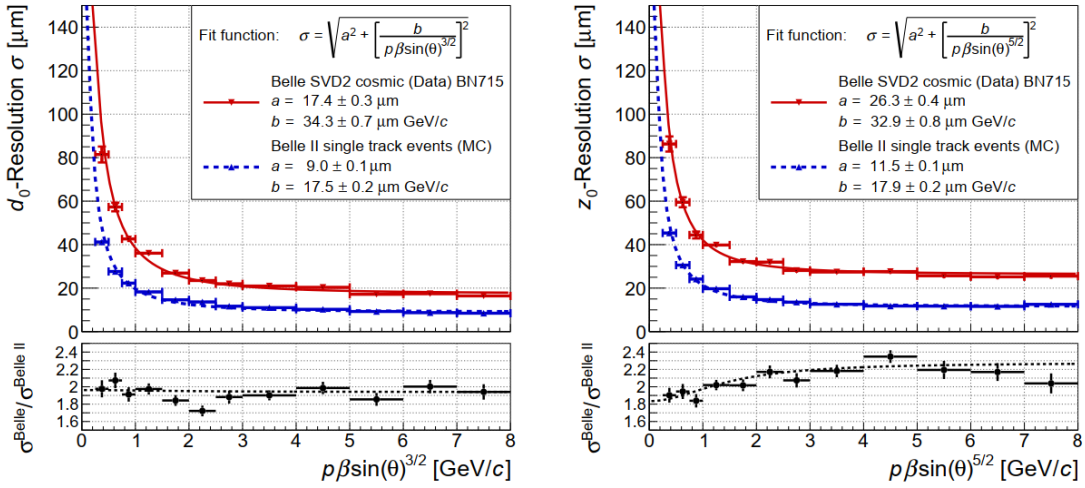

Figure 2.8: Resolution of d_0 (left) and z_0 (right). The results are for MC events with a single muon track using the Belle II tracking algorithm and are compared with the results for Belle cosmic events. [3]

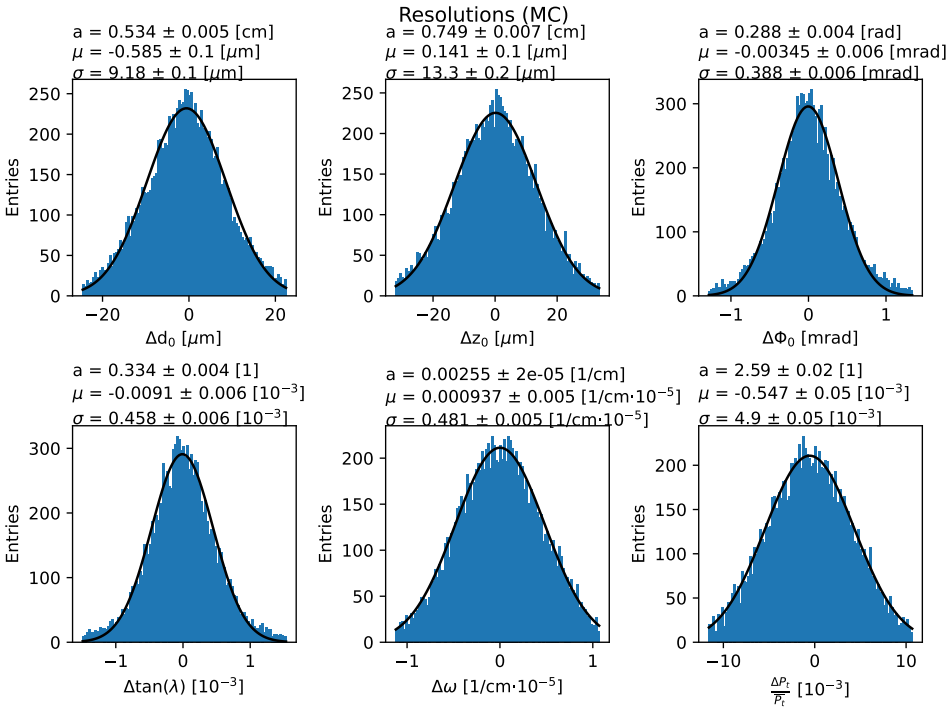

Figure 2.9: Histograms of Δh for MC

We can see that the simulated data is noticeably skewed for Δd and $\frac{\Delta P_t}{P_t}$. For both parameters μ is smaller than σ, so we do not need to take it into account when evaluating the data, but it will contribute to worsening the resolution of the detector. For Δd μ constitutes (6.4 ± 1.1) % of σ and for $\frac{\Delta P_t}{P_t}$ (11.2 ± 1.0)%.

2.3 Correlations of Helix Parameters

We will also make sure the data is not correlated in any way. It is possible for the parameters to be correlated in such a way that the average is zero. If that were the case, our other tests would not find anything wrong with the data, but the resolution would be worse and it could lead to other potential issues when working with the data.

In this section we are the most interested in tracks as close as possible to tracks from collisions. We will achieve this by restricting the data only to tracks passing through the beampipe.

$$|d_0| < 1\,\mathrm{cm}$$

We also remove tracks that pass through the titanium coating of the beampipe, as they will be different from typical physics tracks.

$$-2\,\mathrm{cm} < z_0 < 4\,\mathrm{cm}$$

The correlation plots are done as profile plots. On the y axis we are plotting the mean of all values of Δh from the corresponding bin of h on the x axis. The plots can be seen in Fig. 3.9. We are not using the fit with function 2.3 used in Sect. 2.2, as this would be inefficient. However, this forces us to remove outliers to keep the mean more stable. We could keep the outliers if we used median instead of mean, however, we would be forced to calculate the errors in a different way than 2.4. This would be an unnecessary complication, since the results are the same. Besides, we are only interested in the general correlation of the data and the outliers constitute less than 2% of the chosen data.

The errors were estimated as

$$\sigma_{\Delta h} = \sqrt{\frac{\sigma}{N}} \tag{2.4}$$

where σ is the standard deviation of the data in a bin and N is the number of events in this bin.

We will remove the outliers by choosing only events with:

$$|\Delta d_0| < 100\,\mu\mathrm{m}$$

$$|\Delta z_0| < 200\,\mu\mathrm{m}$$

This leaves us with 66893 events for MC. The correlations can be seen in Fig. 2.10.

In plot Δd vs. ϖ in Fig. 2.10, we can see that Δd is slightly negative for ϖ positive, as this correlation is not symmetrical around zero it could explain the negative bias we see in Fig. 2.9. We have also plotted the same correlations with P_t instead of ω, they can be found in the appendix in Fig. A.4. In Fig. A.4 we can see that $\frac{\Delta P_t}{P_t}$ is negative for all helix parameters, this is a clear reflection of the negative bias we observe in Fig. 2.9. However, it does not tell us much about the origin of this bias as it seems to be the same for all helix parameters.

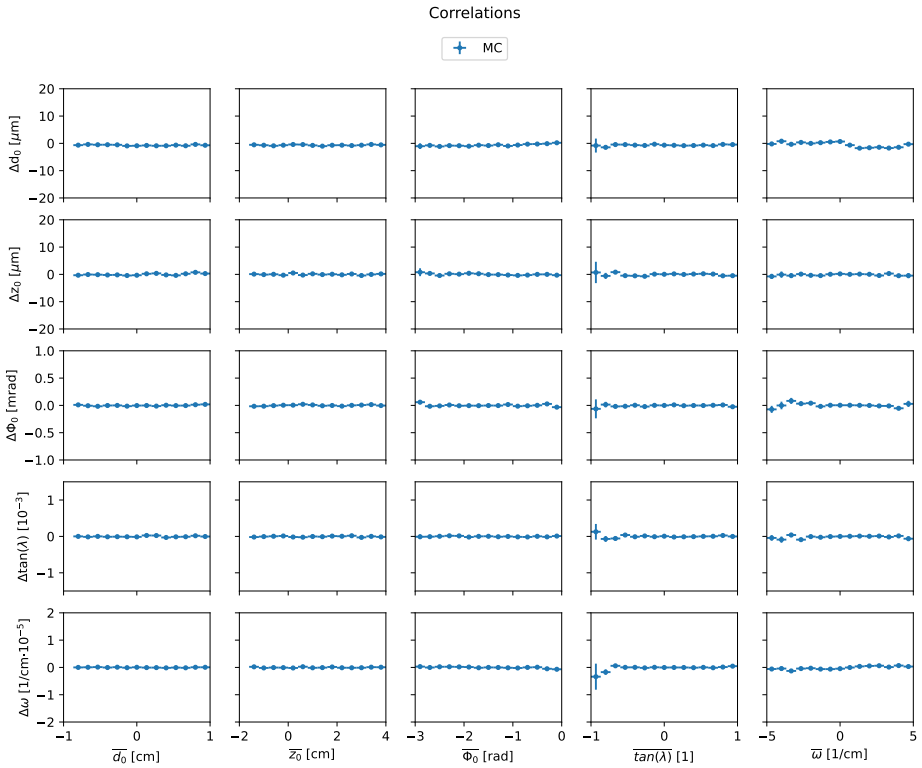

Figure 2.10: Correlations of helix parameters for MC

We also need to make sure that the ranges of correlation plots are chosen well. They have been chosen based on [7], but we can verify it by plotting a 2D histogram of events in those plots and see if most events are in the chosen range. This can be seen in Fig. 2.11

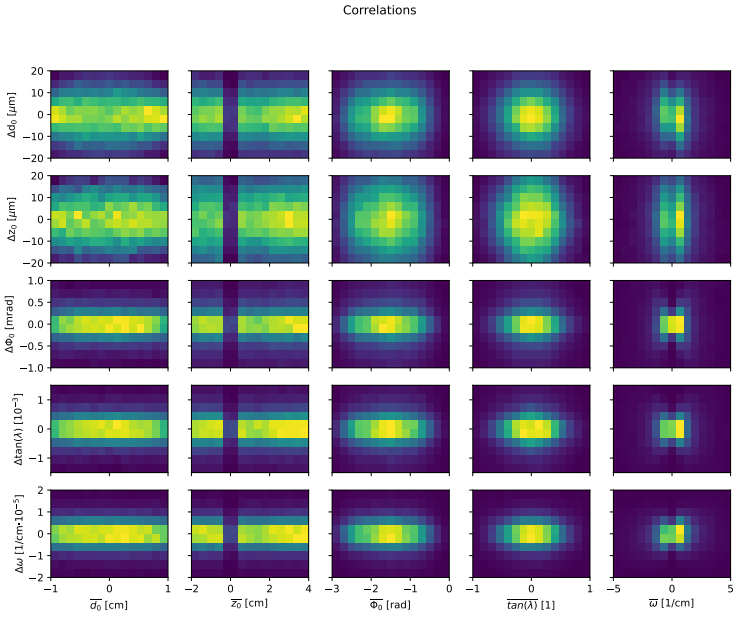

Figure 2.11: 2D histogram for correlations of helix parameters for MC

The lighter colors signify more events in a bin. As we can see, most of the events are centered in all the subplots. For $\overline{d}$ and $\overline{z}$ it might seem as if we need a bigger range, but there are no events beyond this range because of our restriction to use only events passing through the central part of the beampipe.

2.4 Final Resolutions

And finally we can plot the resolution of the detector. We want to be able to apply the resolution found to events from collisions and not just the cosmic muons. Therefore we will again restrict the events only to those passing through the beampipe.

$$|d_0| < 1\,\text{cm}$$

And remove the tracks crossing the titanium coating of the beampipe.

$$-2\,\text{cm} < z_0 < 4\,\text{cm}$$

After this selection we are left with 67590 events. The resolutions will be drawn as a profile plot, similar to correlations in Fig. 2.10. On x axis we are plotting pseudomomentum which is calculated as

$$\tilde{p}_{z_0} = p\beta \sin(\theta)^{\frac{5}{2}} \tag{2.5}$$

for parameters in the longitudinal direction (z_0, $\tan(\lambda)$) and

$$\tilde{p}_{d_0} = p\beta \sin(\theta)^{\frac{3}{2}} \tag{2.6}$$

for parameters in the transversal direction (d_0, ϕ_0).

When calculating pseudomomentum we are assuming the detector is a cylinder and neglecting the slight asymmetry which can be seen in Fig. 1.3. The final formula used is

$$\tilde{p}_{z_0} = p_t\sqrt{1+\tan^2(\lambda)}\frac{1}{\sqrt{\left(1+\frac{0.105^2}{p_t^2(1+\tan^2(\lambda))}\right)}}\frac{1}{(1+\tan^2(\lambda))^{\frac{5}{2}}} \tag{2.7}$$

for parameters in the longitudinal direction (z_0, $\tan(\lambda)$) and

$$\tilde{p}_{d_0} = p_t\sqrt{1+\tan^2(\lambda)}\frac{1}{\sqrt{\left(1+\frac{0.105^2}{p_t^2(1+\tan^2(\lambda))}\right)}}\frac{1}{(1+\tan^2(\lambda))^{\frac{3}{2}}} \tag{2.8}$$

for parameters in the transversal direction (d_0, ϕ_0), where p_t and $\tan(\lambda)$ are the average values for both tracks.

The equations 2.7 and 2.8 have been kept in a non reduced form to make it easier to identify each part with those in equations 2.5, 2.6.

On y axis we are plotting half the distance between 16-th percentile and 84-th percentile (half the range containing 68% of events). We are calculating σ_{68} this way, instead of fitting a Gaussian, to save computation time, since we repeat this calculation for every bin and then repeat the entire process many times to estimate the error. We will determine the error of σ_{68} by bootstrapping. We create new data by randomly sampling the original data with replacement using

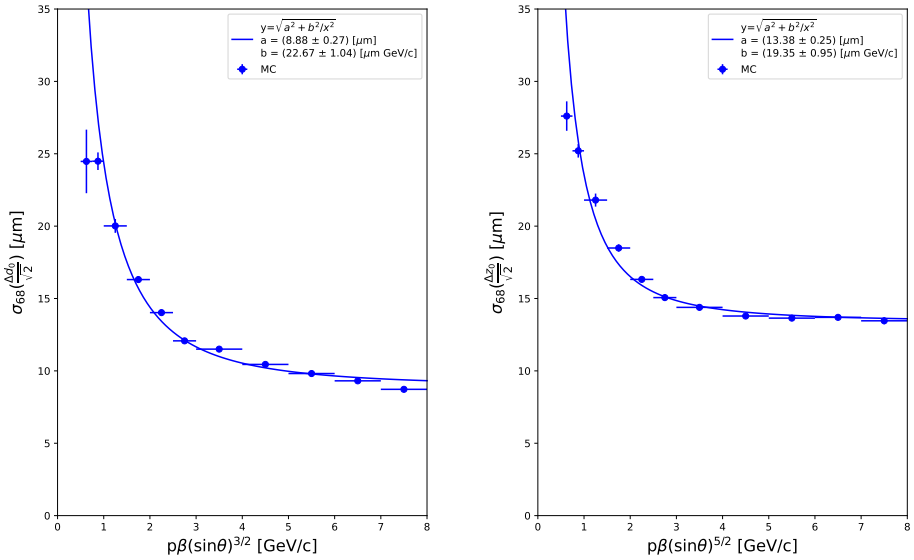

Figure 2.12: Resolutions for d_0 (left) and z_0 (right) for MC

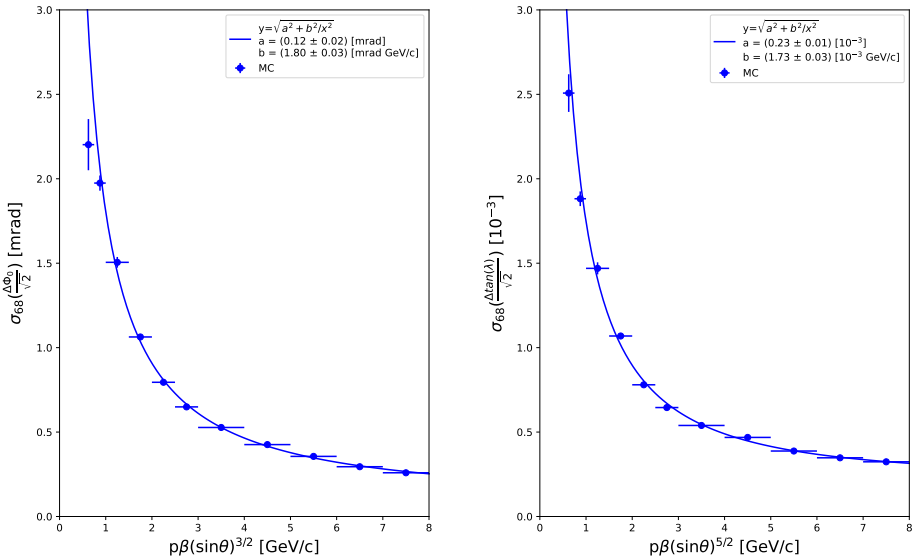

Figure 2.13: Resolutions for ϕ_0 (left) and $\tan(\lambda)$ (right) for MC

the Poisson distribution. After creating 100 data sets using this method, we calculate the error as a standard deviation of the σ_{68} values in each bin.

The resolution plots can be seen in Figs. 2.12, 2.13 and 2.14.

The range was chosen the same as in Fig. 2.8. We use the same binning that was used in Belle internal note #715 without the first bin, since we have only momenta larger than 0.5 GeV/c, as can be seen in Fig. 3.6. The bins are:

$0.5 \sim 0.75 \sim 1.0 \sim 1.5 \sim 2.0 \sim 2.5 \sim 3.0 \sim 4.0 \sim 5.0 \sim 6.0 \sim 7.0 \sim 8.0$

The resolutions were fitted with the function

$$\sigma^2(\tilde{p}) = a^2 + \frac{b^2}{\tilde{p}^2} \tag{2.9}$$

using the least squares method. The a parameter represents the resolution in an infinite momentum limit and the b parameter parameterizes the effect of multiple scattering. For MC the fit parameters are
For d_0:

$$a = 8.88 \pm 0.27[\mu\text{m}]$$

$$b = 22.67 \pm 1.04[\mu\text{m GeV/c}]$$

For z_0:

$$a = 13.38 \pm 0.25[\mu\text{m}]$$

$$b = 19.35 \pm 0.95[\mu\text{m GeV/c}]$$

For ϕ_0:

$$a = 0.12 \pm 0.02[\mu\text{m}]$$

$$b = 1.80 \pm 0.03[\mu\text{m GeV/c}]$$

For $\tan\lambda$:

$$a = 0.23 \pm 0.01[\mu\text{m}]$$

$$b = 1.73 \pm 0.03[\mu\text{m GeV/c}]$$

Additionally the fit parameters can be found in Tables 3.4 and 3.5 where they can be compared with other results.

For P_t the resolution plot is slightly different. We are plotting the resolution of relative P_t vs P_t. The resolution can be seen in Fig. 2.14.

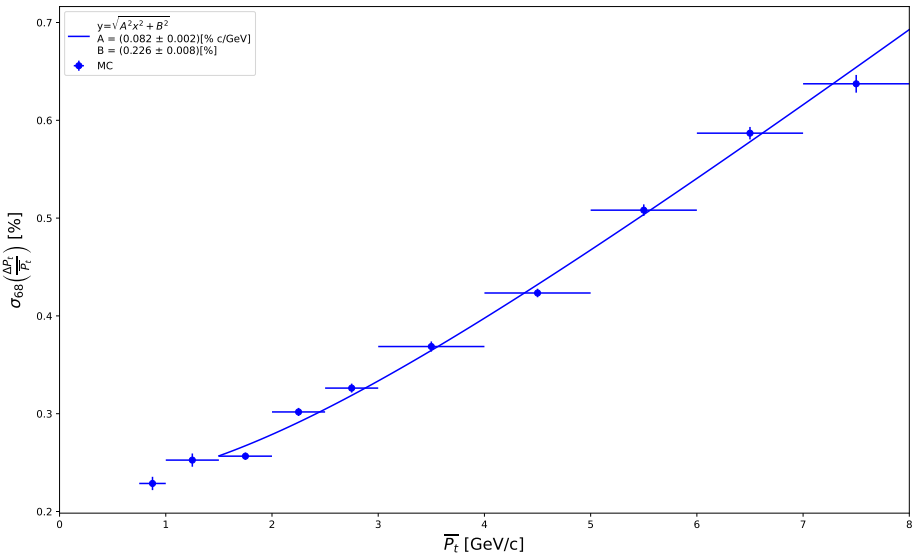

Figure 2.14: Resolution of relative P_t vs average P_t for MC

The resolution in Fig. 2.14 was fitted with a function

$$y = \sqrt{A^2 P_t^2 + B^2} \tag{2.10}$$

The fit parameters are

$$A = 0.082 \pm 0.002[\%\ \mathrm{c/GeV}]$$

$$B = 0.226 \pm 0.008[\%]$$

3. Data from Experiment 12

In this chapter we have two additional data sets available. Prompt = measured data after prompt alignment, and Reprocessing = measured data after reprocessing alignment. The prompt alignment is a preliminary automated alignment done after data taking (in 2020) and the reprocessing alignment was done later in 2021. In the following text we will compare both alignments of the data to MC and prove that Reprocessing is better than Prompt.

3.1 Histograms of Data from Experiment 12

Now we will plot the histograms of data from experiment 12 together with MC. This will allow us to see if the real data is any different than simulation. The histograms can be seen in Figs. 3.1 to 3.6. After using the same restriction as in Sect. 2.1 ($|z_0| > 0.3$ cm) we are left with 133169 events for Prompt and 133325 events for Reprocessing.

On the x axis we are plotting the average of both tracks, calculated as 2.2, on the y axis we are plotting the fraction of events that belong to the bin on x axis.

The Prompt and Reprocessing are not distinguishable but they are both plotted. This similarity makes sense as both Prompt and Reprocessing are just different alignments of the same data.

In Figs. 3.5 to 3.6 we can see slight differences between Monte Carlo and the aligned data. The peaks in fig. 3.5 and 3.3 are sharper for MC. In fig. 3.6 the situation is reversed. The Monte Carlo simulation is not perfect. Outside of the detector the tracks are not simulated as precisely in order to save resources as a result, for lower momenta more particles reach the detector in reality than in simulation (due to scattering and similar effects) and for higher momenta the opposite is true (due to particle showers and other effects). This explains what we see in Fig. 3.6. We will be focusing on higher momenta events where the differences between MC and data are not as significant.

3.2 Resolutions for a Range of Momenta for Data from Experiment 12

We will again only analyze events with momenta in the range 4 GeV/c to 5 GeV/c. For completeness the histograms for all events (no P_t restriction) can be found in appendix (Figs. A.3 to A.6).

The results from plotting all events are very similar to our selection. This is not surprising, since, as we said earlier, the muons from cosmic rays carry much higher momentum than particles from collisions and are less affected by multiple scattering. From Fig. 3.6 we can see that most of our events have high momenta, thus the average is close to the results from our P_t selection.

Again the fit was done using the function 2.3. The parameters μ and σ can be found in Tables 3.1 to 3.3, as well as the bias μ as a percentage of the resolution σ (calculated as $\frac{|\mu|}{\sigma}$).

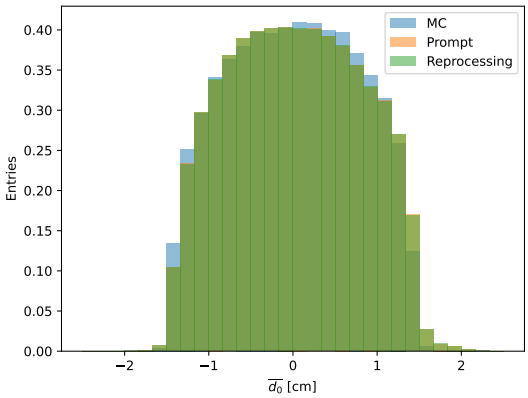

Figure 3.1: Histogram of $\overline{d_0}$

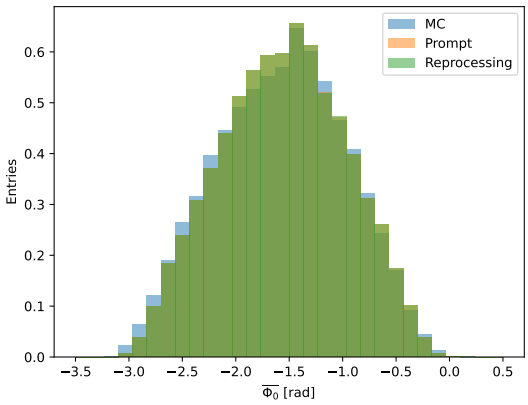

Figure 3.2: Histogram of $\overline{\phi_0}$

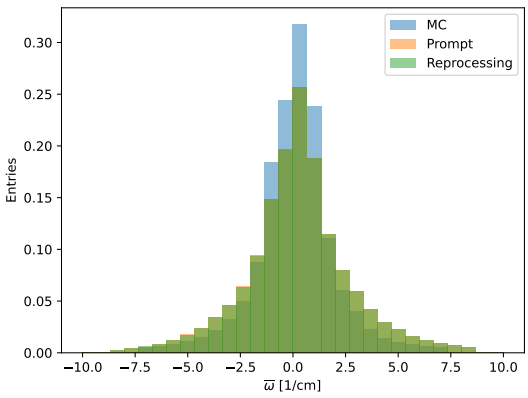

Figure 3.3: Histogram of $\overline{\omega}$

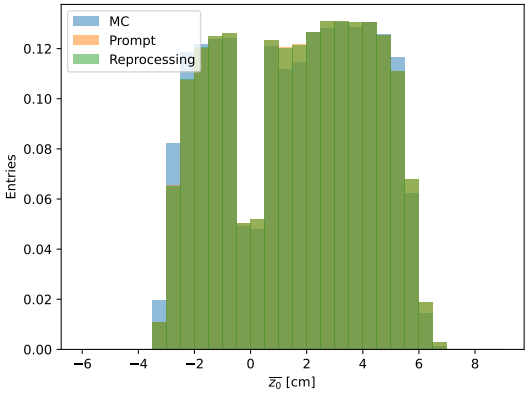

Figure 3.4: Histogram of $\overline{z_0}$

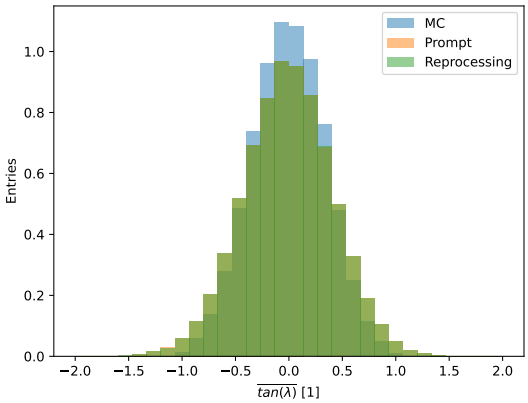

Figure 3.5: Histogram of $\overline{\tan(\lambda)}$

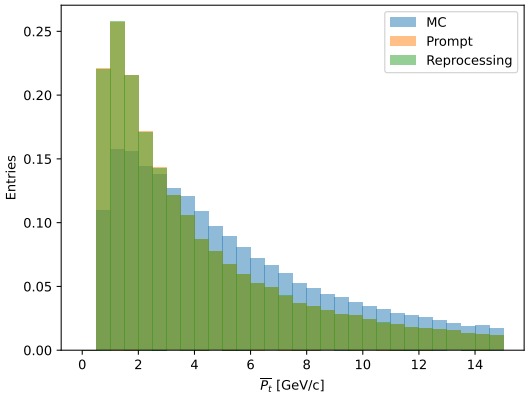

Figure 3.6: Histogram of $\overline{P_t}$

The errors in Tables 3.1, 3.2, 3.3 for $\frac{|\mu|}{\sigma}$ were calculated as

$$\sigma_{|\mu|/\sigma} = 100\sqrt{\left(\frac{\sigma_\mu}{\sigma}\right)^2 + \left(\frac{\mu\sigma_\sigma}{\sigma^2}\right)^2} \tag{3.1}$$

where σ_μ and σ_σ are errors of μ and σ respectively. We omitted the parameter a as it si not that interesting for our analysis and changes drastically with the number of bins.

Again we can observe that μ is always at least one order of magnitude smaller than σ. Which means that the data is not significantly skewed. However, the fact

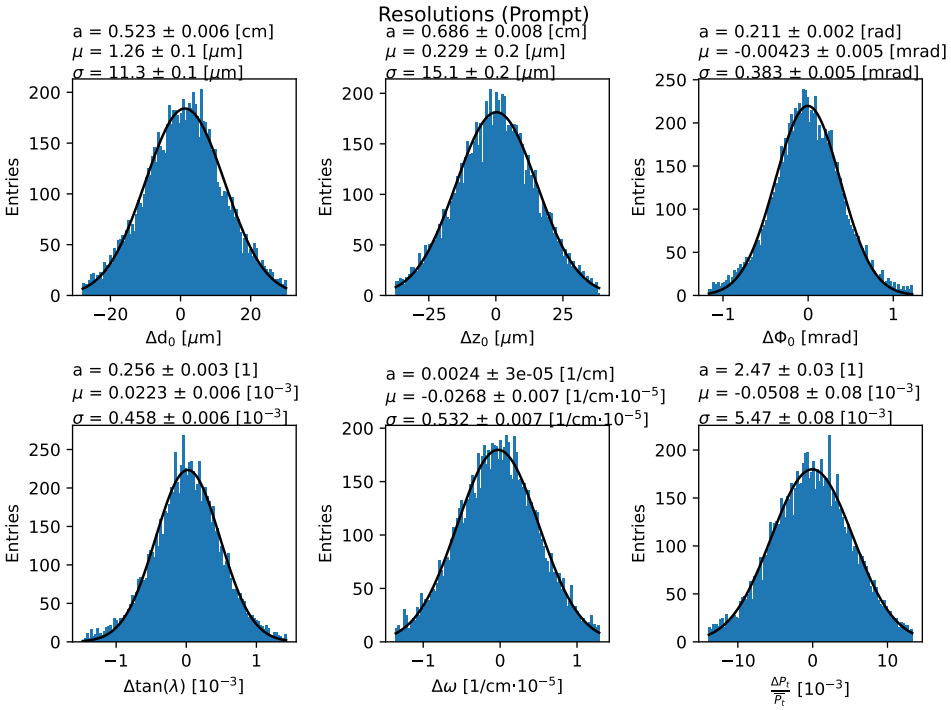

Figure 3.7: Histograms of Δh for Prompt

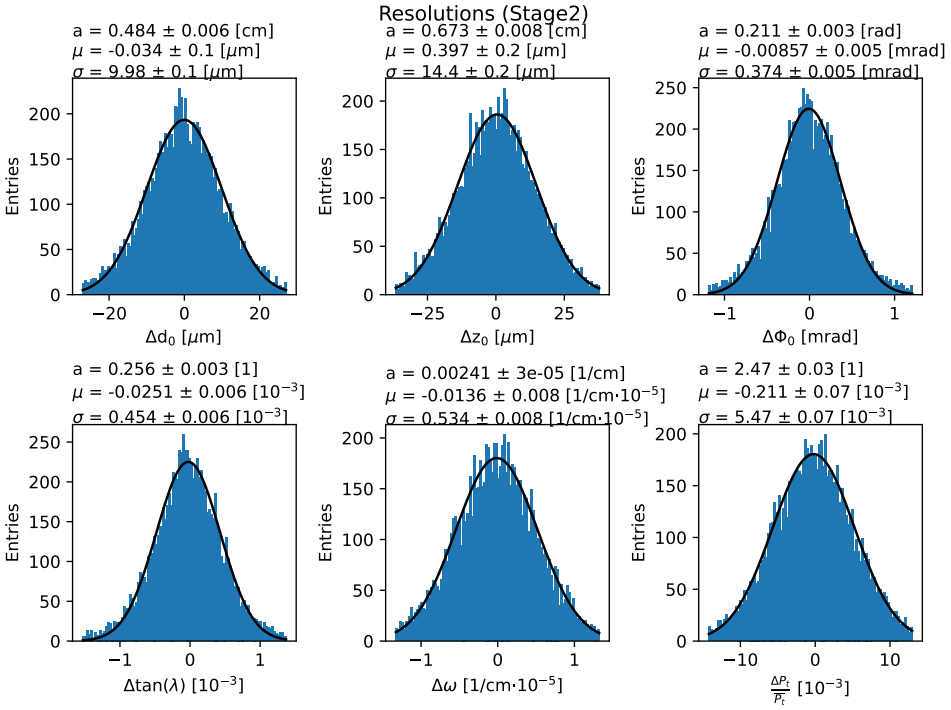

Figure 3.8: Histograms of Δh for Stage2

Table 3.1: Resolution fit parameters for MC

Helix parameter	μ	σ	$\frac{\lvert\mu\rvert}{\sigma}$ [%]
d_0 [μm]	-0.6 ± 0.1	9.2 ± 0.1	6.4 ± 1.1
z_0 [μm]	0.1 ± 0.1	13.3 ± 0.2	1.1 ± 0.8
ϕ [mrad]	-0.003 ± 0.006	0.388 ± 0.006	0.9 ± 1.5
$\tan\lambda$ [10^{-3}]	-0.009 ± 0.006	0.458 ± 0.006	2.0 ± 1.3
ω [10^{-5}/cm]	0.001 ± 0.005	0.481 ± 0.005	0.2 ± 1.0
$\frac{\Delta P_t}{P_t}$ [10^{-3}]	-0.55 ± 0.05	4.90 ± 0.05	11.2 ± 1.0

Table 3.2: Resolution fit parameters for Prompt

Helix parameter	μ	σ	$\frac{\lvert\mu\rvert}{\sigma}$ [%]
d_0 [μm]	1.3 ± 0.1	11.3 ± 0.1	11.2 ± 0.9
z_0 [μm]	0.2 ± 0.2	15.1 ± 0.1	1.5 ± 1.3
ϕ [mrad]	-0.004 ± 0.005	0.383 ± 0.005	1.1 ± 1.3
$\tan\lambda$ [10^3]	0.022 ± 0.006	0.458 ± 0.006	4.9 ± 1.3
ω [10^5/cm]	-0.027 ± 0.007	0.532 ± 0.007	5.0 ± 1.3
$\frac{\Delta P_t}{P_t}$ [10^3]	-0.05 ± 0.08	5.47 ± 0.08	0.9 ± 1.5

Table 3.3: Resolution fit parameters for Reprocessing

Helix parameter	μ	σ	$\frac{\lvert\mu\rvert}{\sigma}$ [%]
d_0 [μm]	-0.0 ± 0.1	10.0 ± 0.1	0.3 ± 1.0
z_0 [μm]	0.4 ± 0.2	14.4 ± 0.2	2.8 ± 1.4
ϕ [mrad]	-0.009 ± 0.005	0.374 ± 0.005	2.2 ± 1.3
$\tan\lambda$ [10^3]	-0.025 ± 0.006	0.454 ± 0.006	5.5 ± 1.3
ω [10^5/cm]	-0.014 ± 0.008	0.534 ± 0.008	2.5 ± 1.5
$\frac{\Delta P_t}{P_t}$ [10^3]	-0.21 ± 0.07	5.47 ± 0.07	3.9 ± 1.3

that some of the data is skewed should not be neglected. For Prompt the bias is even worse for d than for MC but surprisingly disappears for P_t. $\tan\lambda$ and ω are also skewed but to a lesser extent . And finally for Reprocessing z_0, ϕ_0, $\tan\lambda$ and ω are all slightly worse than MC, but d_0 is almost perfectly centered, and P_t is much better than MC but a little bit worse than Prompt.

The fact that MC is so skewed for P_t seems to be an issue with the Monte Carlo simulation. For d_0 for Prompt and MC the bias could be explained by a correlation of helix parameters, which can be seen in Fig. 3.9. The results stay mostly the same if we change the number of bins or if we do not restrict the momenta and plot all events (Figs. A.3 to A.6).

3.3 Correlations of Helix Parameters for Data from Experiment 12

Here we use the same restriction as in Sect. 2.3. This leaves us with 67621 events for Prompt and 67739 for Reprocessing.

In Fig. 3.9 we can see that for MC and Stage2 no helix parameters are

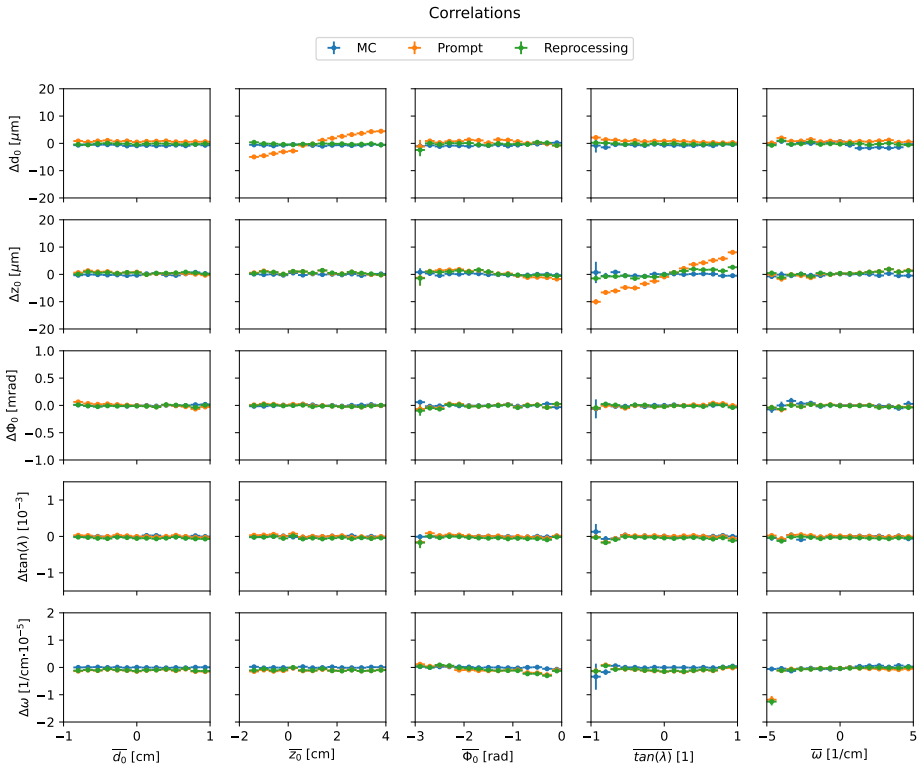

Figure 3.9: Correlations of helix parameters

correlated, however, for Prompt Δd_0 is correlated to $\overline{z_0}$ and Δz_0 is correlated to $\tan\lambda$. For Prompt the correlation of Δd_0 and $\overline{z_0}$ is not centered on $\overline{z_0} = 0$, which could explain the bias we see for Δd_0 in Table 3.2.

Here we see the first difference between Prompt alignment and Reprocessing. In the next section we will see that this 'small' change in correlations will lead to significant improvement in resolution. However, Reprocessing is still not perfect, we can see that for positive $\tan\lambda$ the correlation of Δz_0 remains, although significantly reduced. From Table 3.3 we can see that the bias for Δz_0 is negligible. The negative bias for $\tan\lambda$ we can see in this table is not visible in Fig. 3.9 and it is probably caused by a different effect.

In Fig. A.7 we can see the correlations with P_t instead of ω. There we can see that the bias seen for MC is no longer present for Prompt and Reprocessing. However, it is possible that the issue lies deeper and the alignment simply adds a constant value to offset this bias. We have not further studied the origin of this bias for MC.

3.4 Final Resolutions for Data from Experiment 12

Finally we get to the resolution of helix parameters. Again we are using only the tracks passing through the beampipe, the same as in Sect. 2.4. For Prompt we have 68912 events and 69016 for Reprocessing.

The resolution plots can be seen in Figs. 3.10 and 3.11.

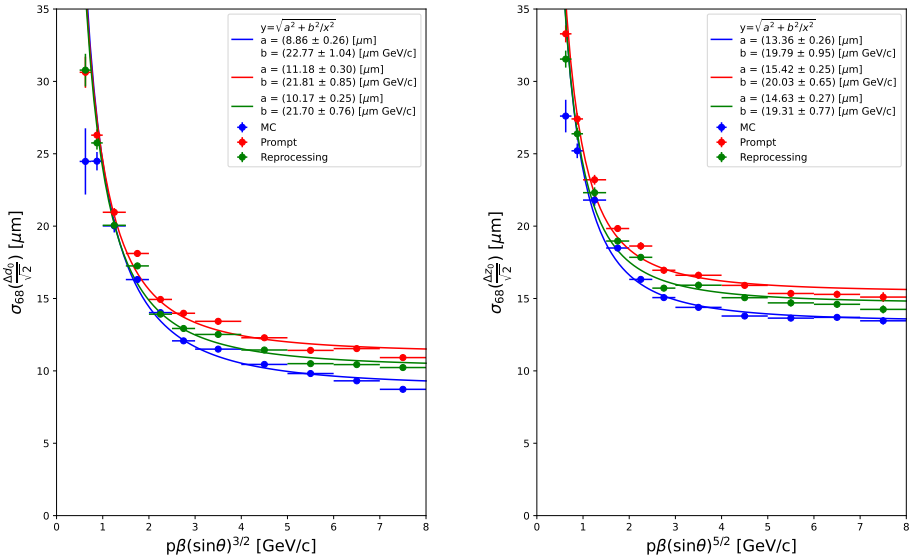

Figure 3.10: Resolutions for d_0 (left) and z_0 (right)

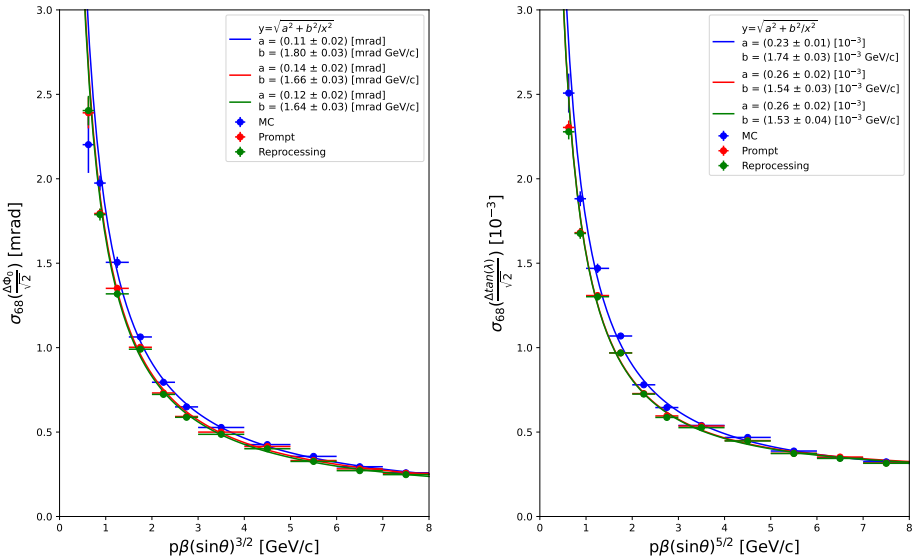

Figure 3.11: Resolutions for ϕ_0 (left) and $\tan(\lambda)$ (right)

The fit parameters and their statistical errors can be found in Tables 3.4 and 3.5.

We can see that for both d_0 and z_0 Reprocessing is a significant improvement to Prompt, however, it does not reach the theoretical resolution provided by Monte Carlo simulation. That is expected since there are always some effects not accounted for in the simulation.

For ϕ_0 and $\tan\lambda$ the resolutions are the same for Prompt and Reprocessing, but the effect of scattering is worse for MC (parameter b). The difference is very

Table 3.4: Parameter a for final resolution fit

Helix parameter	MC	Prompt	Reprocessing
d_0 [μm]	8.88 ± 0.27	11.18 ± 0.30	10.17 ± 0.25
z_0 [μm]	13.38 ± 0.25	15.42 ± 0.25	14.63 ± 0.27
ϕ_0 [mrad]	0.12 ± 0.02	0.14 ± 0.02	0.12 ± 0.02
$\tan\lambda$ [10^{-3}]	0.23 ± 0.01	0.26 ± 0.02	0.26 ± 0.02

Table 3.5: Parameter b for final resolution fit

Helix parameter	MC	Prompt	Reprocessing
d_0 [μm GeV/c]	22.67 ± 1.04	21.81 ± 0.85	21.70 ± 0.76
z_0 [μm GeV/c]	19.35 ± 0.95	20.03 ± 0.65	19.31 ± 0.77
ϕ_0 [mrad GeV/c]	1.80 ± 0.03	1.66 ± 0.03	1.64 ± 0.03
$\tan\lambda$ [10^{-3} GeV/c]	1.73 ± 0.03	1.54 ± 0.03	1.53 ± 0.04

small and it could be caused by multiple effects. For example the difference in small P_t between data and simulation (seen in Fig. 3.6) could be responsible.

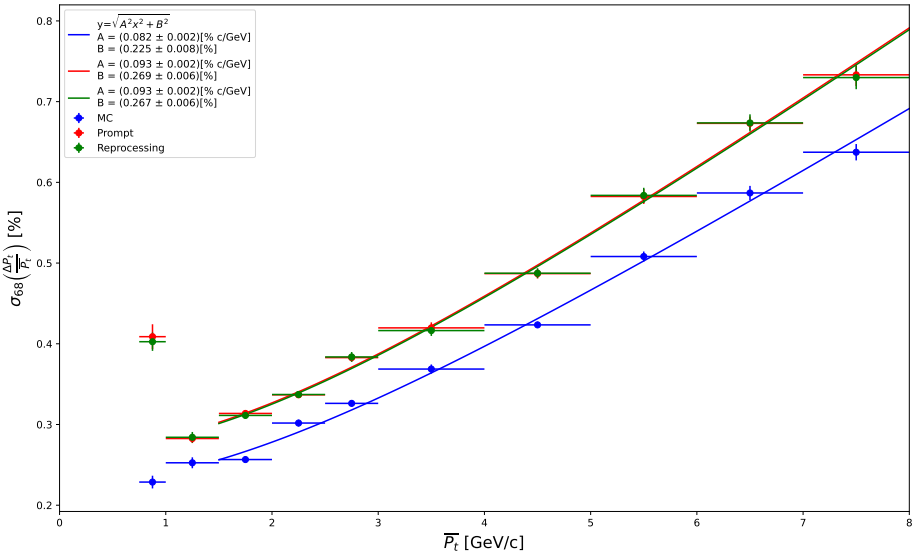

Figure 3.12: Resolutions of relative P_t vs average P_t

The fit parameters are for Prompt:

$$A = 0.093 \pm 0.002 \text{ [\% c/GeV]}$$

$$B = 0.269 \pm 0.006 \text{ [\%]}$$

and for Reprocessing:

$$A = 0.093 \pm 0.002 \text{ [\% c/GeV]}$$

$$B = 0.267 \pm 0.006 \text{ [\%]}$$

Now we will examine one source of systematic error. The range of the resolution graphs was chosen based on [3], but if we extend this range and use more points for the fit, we will get slightly different results. We will extend the range to 15 GeV/c, as beyond this point we have only a small number of events in each bin. This can be seen in Fig. 3.6. For this range the fit parameters can be found in Tables 3.6 and 3.7. The extended resolutions can be seen in Figs. A.8, A.9 and A.10

Table 3.6: Parameter a for estimating the systematic error

Helix parameter	MC	Prompt	Reprocessing
d_0 [μm]	8.35 ± 0.20	10.76 ± 0.22	9.74 ± 0.20
z_0 [μm]	13.20 ± 0.18	15.20 ± 0.18	14.50 ± 0.19
ϕ_0 [mrad]	0.09 ± 0.01	0.12 ± 0.01	0.12 ± 0.01
$\tan\lambda$ [10^{-3}]	0.22 ± 0.01	0.25 ± 0.01	0.24 ± 0.01

Table 3.7: Parameter b for estimating the systematic error

Helix parameter	MC	Prompt	Reprocessing
d_0 [μm GeV/c]	23.89 ± 0.99	22.39 ± 0.74	22.37 ± 0.71
z_0 [μm GeV/c]	20.12 ± 0.74	20.31 ± 0.54	19.49 ± 0.60
ϕ_0 [mrad GeV/c]	1.82 ± 0.02	1.67 ± 0.02	1.64 ± 0.02
$\tan\lambda$ [10^{-3} GeV/c]	1.75 ± 0.02	1.56 ± 0.03	1.55 ± 0.03

And for the relative P_t resolution we have: for MC:

$$A = 0.076 \pm 0.002 \text{ [\% c/GeV]}$$

$$B = 0.240 \pm 0.009 \text{ [\%]}$$

for Prompt:

$$A = 0.088 \pm 0.002 \text{ [\% c/GeV]}$$

$$B = 0.280 \pm 0.008 \text{ [\%]}$$

and for Reprocessing:

$$A = 0.088 \pm 0.002 \text{ [\% c/GeV]}$$

$$B = 0.279 \pm 0.008 \text{ [\%]}$$

Other sources of systematic error are the binning used and the method used for the fit. We will not be evaluating the errors from these sources because the binning used was chosen the same as Belle internal note #715 for easier comparison with other Belle II documents.

The resolutions with the systematic error caused by the range of the resolution graphs are in Tables 3.8, 3.9 and below them for P_t.

And for the relative P_t resolution we have: for MC:

$$A = 0.082 \pm 0.002 \pm 0.06 \text{ [\% c/GeV]}$$

$$B = 0.225 \pm 0.008 \pm 0.15 \text{ [\%]}$$

Table 3.8: Parameter a with systematic error

Helix param.	MC	Prompt	Reprocessing
d_0 [μm]	$8.88 \pm 0.27 \pm 0.53$	$11.18 \pm 0.30 \pm 0.42$	$10.17 \pm 0.25 \pm 0.43$
z_0 [μm]	$13.38 \pm 0.25 \pm 0.18$	$15.42 \pm 0.25 \pm 0.22$	$14.63 \pm 0.27 \pm 0.13$
ϕ_0 [mrad]	$0.12 \pm 0.02 \pm 0.03$	$0.14 \pm 0.02 \pm 0.02$	$0.12 \pm 0.02 \pm 0.00$
$\tan\lambda$ [10^{-3}]	$0.23 \pm 0.01 \pm 0.01$	$0.26 \pm 0.02 \pm 0.01$	$0.26 \pm 0.02 \pm 0.02$

Table 3.9: Parameter b with systematic error

Helix param.	MC	Prompt	Reprocessing
d_0 [μm GeV/c]	$22.67 \pm 1.04 \pm 1.22$	$21.81 \pm 0.85 \pm 0.58$	$21.70 \pm 0.76 \pm 0.67$
z_0 [μm GeV/c]	$19.35 \pm 0.95 \pm 0.77$	$20.03 \pm 0.65 \pm 0.28$	$19.31 \pm 0.77 \pm 0.18$
ϕ_0 [mrad GeV/c]	$1.80 \pm 0.03 \pm 0.02$	$1.66 \pm 0.03 \pm 0.01$	$1.64 \pm 0.03 \pm 0.00$
$\tan\lambda$ [10^{-3} GeV/c]	$1.73 \pm 0.03 \pm 0.02$	$1.54 \pm 0.03 \pm 0.02$	$1.53 \pm 0.04 \pm 0.02$

for Prompt:

$$A = 0.093 \pm 0.002 \pm 0.05 \text{ [\% c/GeV]}$$

$$B = 0.269 \pm 0.006 \pm 0.11 \text{ [\%]}$$

and for Reprocessing:

$$A = 0.093 \pm 0.002 \pm 0.05 \text{ [\% c/GeV]}$$

$$B = 0.267 \pm 0.006 \pm 0.12 \text{ [\%]}$$

4. Data from Experiments 20 to 24

We also have newer data available. The data is from 29.10.2021 to 30.3.2022. The gathering of the data was interrupted several times for maintenance breaks and Christmas holidays. It is thus separated into buckets 27 to 31, each bucket represents approximately 14 days of data (except bucket27 and bucket29). For this data we do not have Monte Carlo simulation or prompt alignment available. As we have only the reprocessing alignment data (the same alignment as Reprocessing for data from experiment 12), we can only compare the buckets with each other or with Reprocessing from previous section.

4.1 Comparison of the Buckets

After removing the events from collisions ($|z_0| > 0.3$ cm) we have the following number of events in the buckets:
bucket27: 18214
bucket28: 12212
bucket29: 8189
bucket30: 11551
bucket31: 10480
60646 events in total. That is less than half the events we had in the previous section. As each bucket represents only a small statistical sample we will only quickly compare them to see if there are any significant differences between them and the merge them into one dataset for better statistical results.

There are no noticeable oddities in histograms for the buckets as can be seen in Figs. 4.1 to 4.6.

No significant correlations for the helix parameters can be seen in Fig. 4.7.

There is very little data to properly analyze the histograms of Δh as we did in Sect. 2.2 because after restricting the momentum to 4 GeV/c $\sim$ 5 GeV/c we are left with less than 1000 events for each bucket, the number of bins was reduced to 50 from 100. The results can be seen in Figs. A.11 to A.15 in appendix. The most significant biases are presented in Table 4.1. From Table 4.1 we can see that for $\tan\lambda$ we are getting consistently bad results, bucket30 is especially bad, but some of this can be attributed to small sample size and unfortunate binning.

We can also compare the resolutions for the buckets. It can be seen in Fig. 4.8.

We can see that while not identical for all the buckets, the d_0 and z_0 resolutions are very similar and there is no noticeable trend of increasing or decreasing resolution for newer data. For ϕ_0 and $\tan\lambda$ the resolutions are not sown because the buckets are indistinguishable from each other and the resolutions for merged buckets will be shown later.

The comparisons of the parameters a for d_0, z_0 and B for P_t are in Fig. 4.9. We can see that the resolution seems to be getting worse for relative P_t, but it is impossible to tell for certain with this small sample.

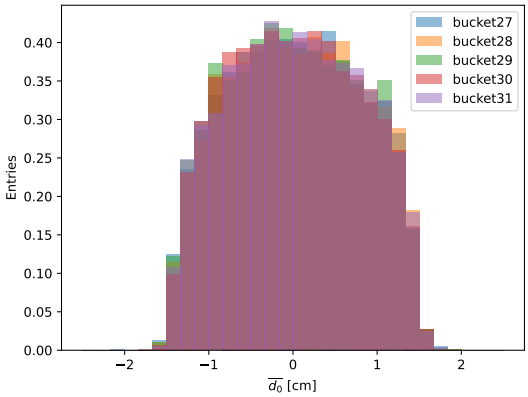

Figure 4.1: Histogram of $\overline{d_0}$

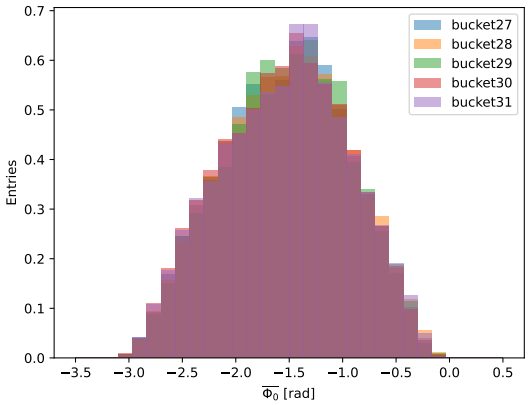

Figure 4.2: Histogram of $\overline{\phi_0}$

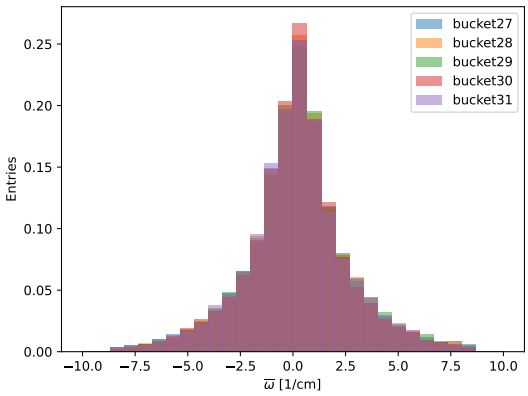

Figure 4.3: Histogram of $\overline{\omega}$

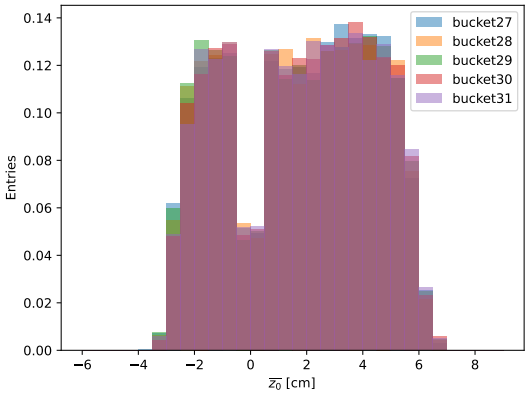

Figure 4.4: Histogram of $\overline{z_0}$

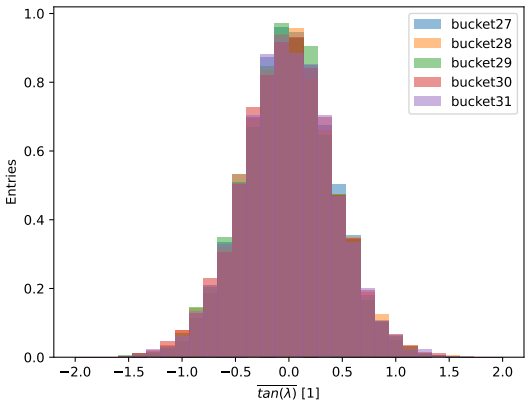

Figure 4.5: Histogram of $\overline{\tan(\lambda)}$

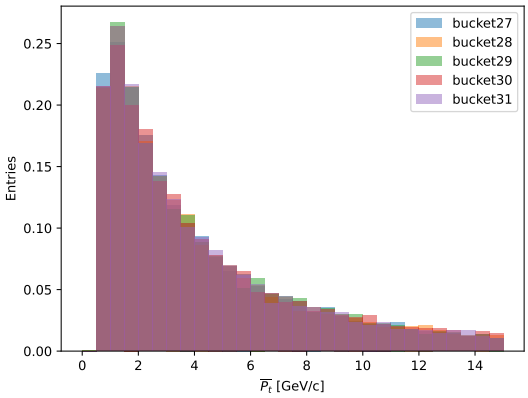

Figure 4.6: Histogram of $\overline{P_t}$

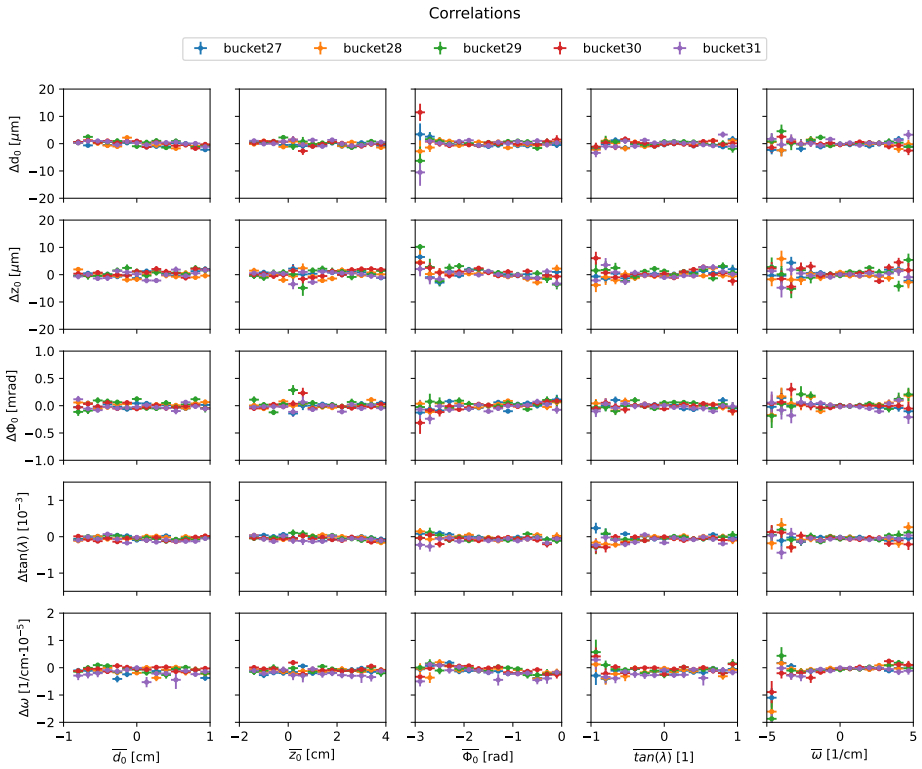

Figure 4.7: Correlations of helix parameters

Table 4.1: Most significant biases for each bucket

buckets	parameters	$\frac{\lvert\mu\rvert}{\sigma}$ [%]
bucket27	d_0	4.23 ± 2.7
	z_0	5.93 ± 2.88
	ω	10.1 ± 4.49
bucket28	$\tan\lambda$	9.42 ± 3.98
	ω	7.45 ± 4.08
bucket29	$\tan\lambda$	10.3 ± 4.41
bucket30	$\tan\lambda$	22.2 ± 4.93
	P_t	10.3 ± 3.78
bucket31	$\tan\lambda$	10.5 ± 3.68

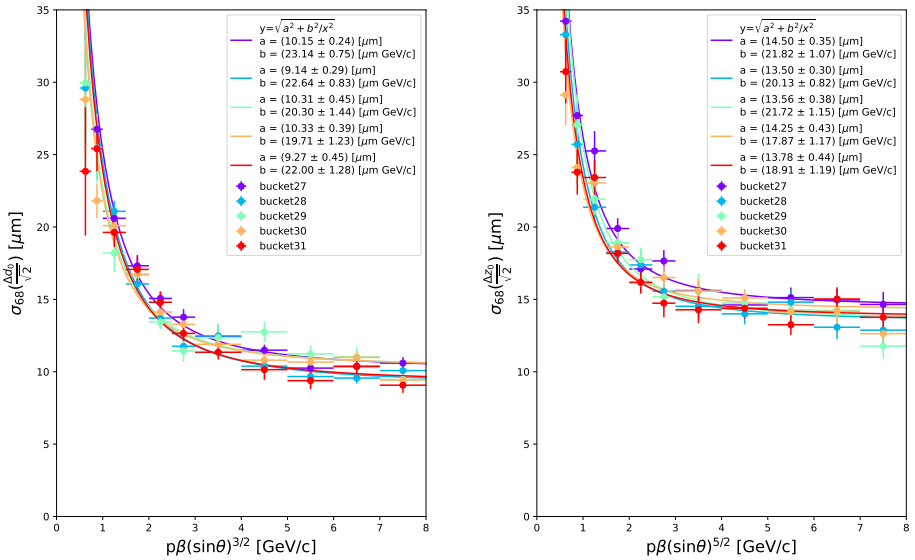

Figure 4.8: Resolutions for d_0 (left) and z_0 (right)

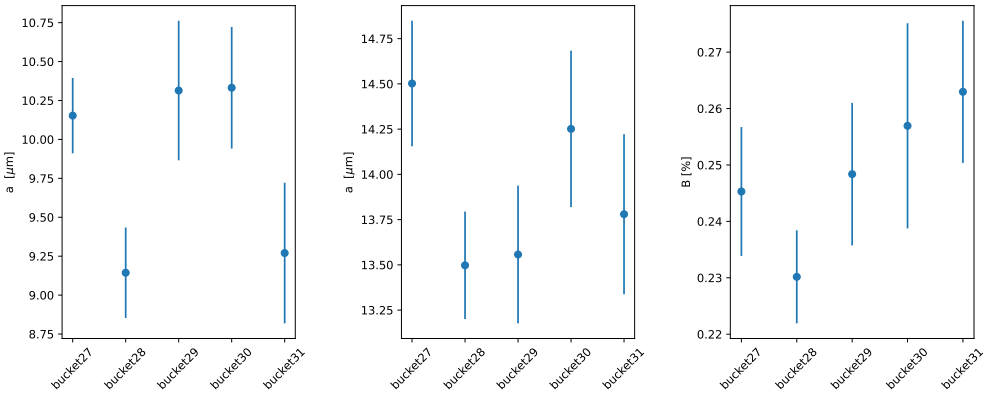

Figure 4.9: Comparison of a parameters for d_0 (left), z_0 (middle) and B for P_t (right)

4.2 Merged Data

Now that we made sure that none of the buckets are unusual in any way we can merge the data and compare it with results from chapter 3.

If we compare the distributions of helix parameters for merged buckets (All_buckets) and Reprocessing from previous chapter (Figs. 4.10 to 4.15), we can see that there are no significant differences between them. This means that there have not been any big changes to the detector or our source of particles. Muons from cosmic rays recorded during collisions in a specialized skim may for example be affected by changed trigger configuration.

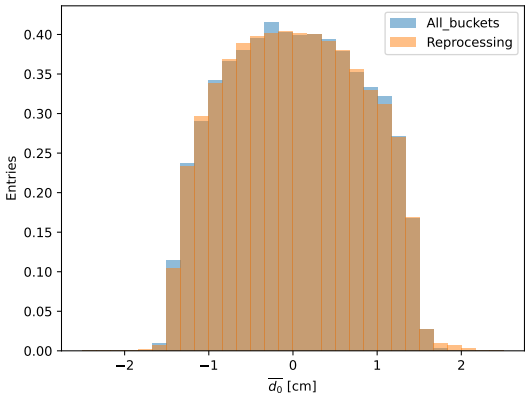

Figure 4.10: Histogram of $\overline{d_0}$

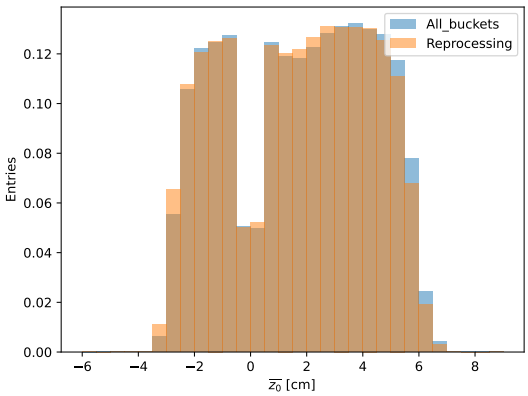

Figure 4.13: Histogram of $\overline{z_0}$

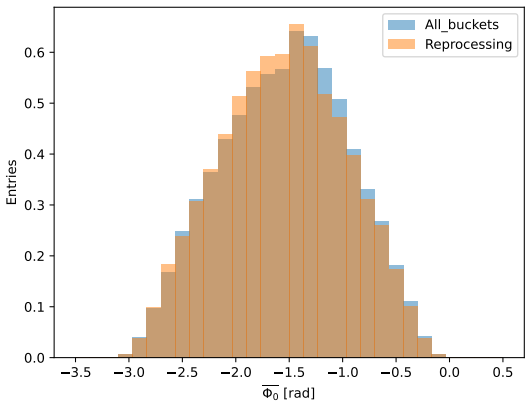

Figure 4.11: Histogram of $\overline{\phi_0}$

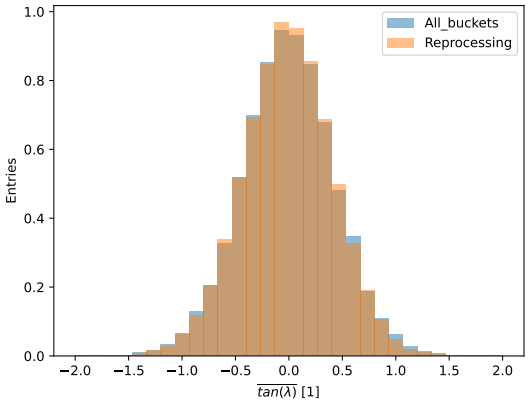

Figure 4.14: Histogram of $\overline{\tan(\lambda)}$

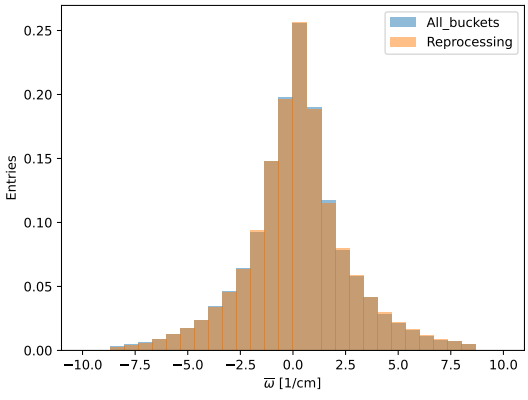

Figure 4.12: Histogram of $\overline{\omega}$

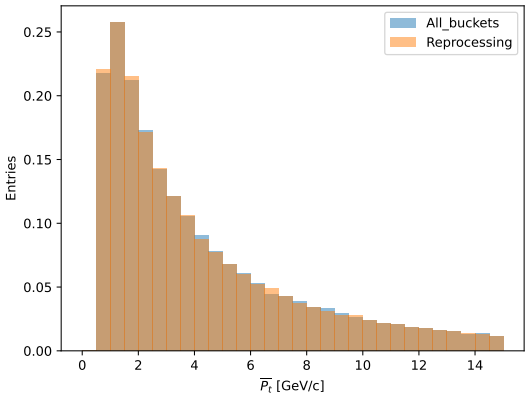

Figure 4.15: Histogram of $\overline{P_t}$

After merging the data from all buckets we have enough events to properly check if the data is skewed in any way. When plotting the histograms of Δh we will use the same restrictions to our data as in Sect. 2.2. The histograms can bee seen in Fig. 4.16.

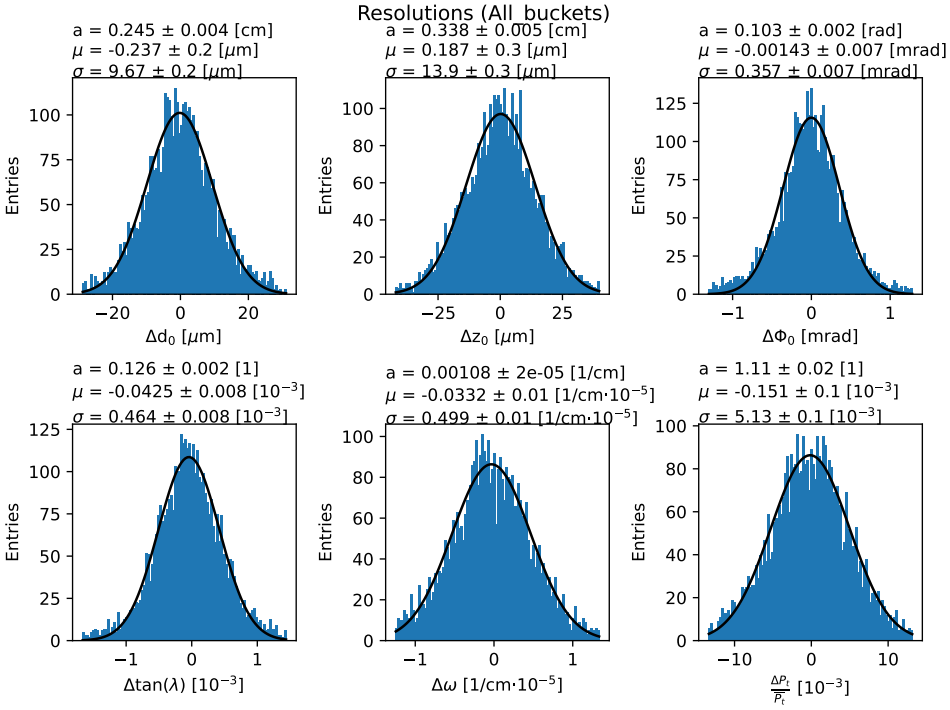

Figure 4.16: Histograms of Δh for merged buckets

Table 4.2: Resolution fit parameters for merged buckets

Helix parameter	μ	σ	$\frac{\lvert\mu\rvert}{\sigma}$ [%]
d_0 [μm]	-0.2 ± 0.2	9.7 ± 0.2	2.5 ± 1.9
z_0 [μm]	0.2 ± 0.3	13.9 ± 0.3	1.3 ± 1.9
ϕ [mrad]	-0.001 ± 0.007	0.357 ± 0.007	0.4 ± 2.0
$\tan\lambda$ [10^{-3}]	-0.043 ± 0.008	0.464 ± 0.008	9.2 ± 1.7
ω [10^{-5}/cm]	-0.03 ± 0.01	0.50 ± 0.01	6.7 ± 2.0
$\frac{\Delta P_t}{P_t}$ [10^{-3}]	-0.2 ± 0.1	5.1 ± 0.1	2.9 ± 1.9

From Table 4.2 we can see that the biases for merged buckets are similar to Reprocessing, except for $\tan\lambda$ where we have much worse result. ω is also worse but not significantly.

If we plot correlations in Fig. 4.17, we see that there are no big differences between new data and Reprocessing. The only noticeable difference is the Δz_0 x $\tan\lambda$ where it seems like we have better results for new data than for Reprocessing. We are again using the same restrictions as in Sect. 3.3.

Now we will plot the final resolutions. Again everything except the new data is the same as in Sect. 3.4. We are left with 31178 for All_buckets. The fit parameters for the resolutions are presented in Tables 4.3 and 4.4.

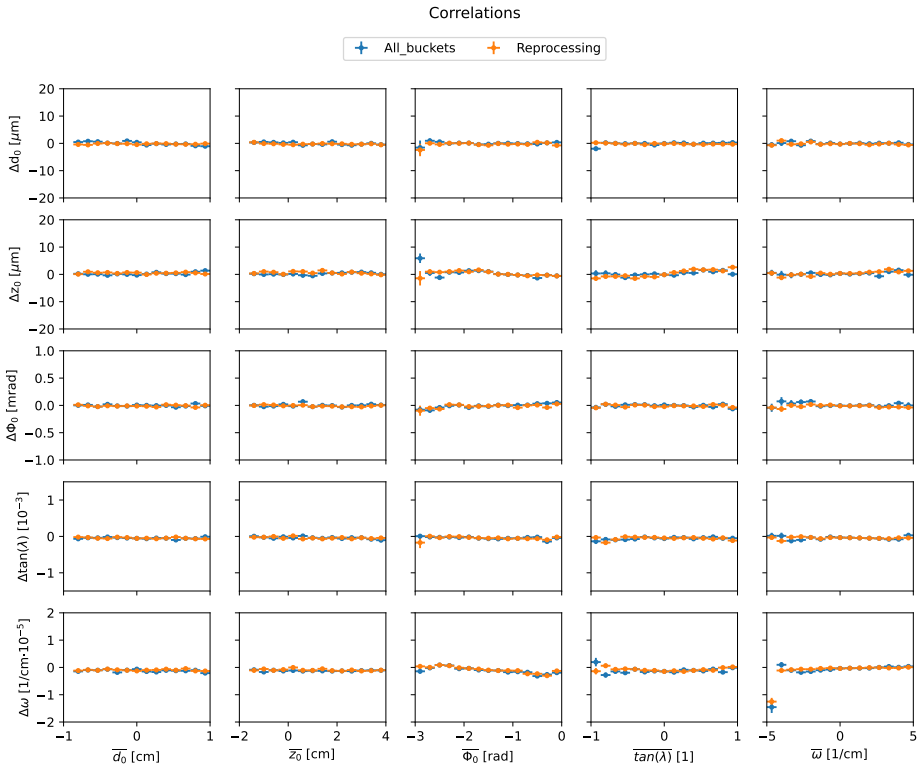

Figure 4.17: Correlations of helix parameters

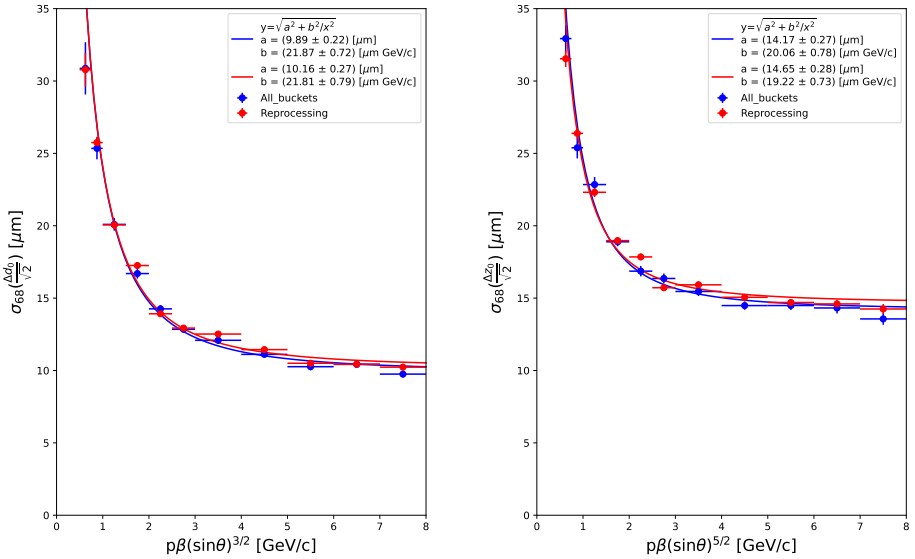

Figure 4.18: Resolutions for d_0 (left) and z_0 (right)

We can see that the ϕ_0 and $\tan(\lambda)$ resolutions are identical for both data. For d_0 and z_0 it seems like the resolution for All_buckets is slightly better, but if we take into account both errors they are again identical.

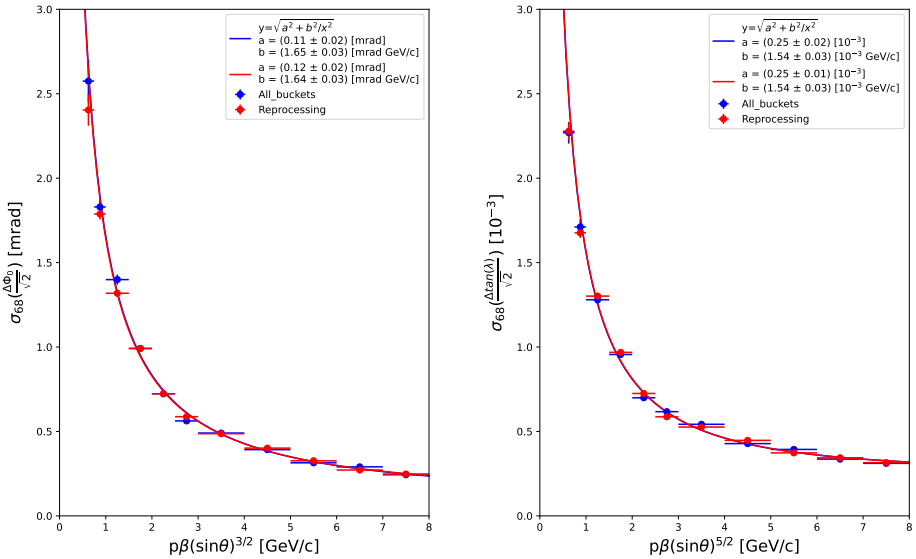

Figure 4.19: Resolutions for ϕ_0 (left) and $\tan(\lambda)$ (right)

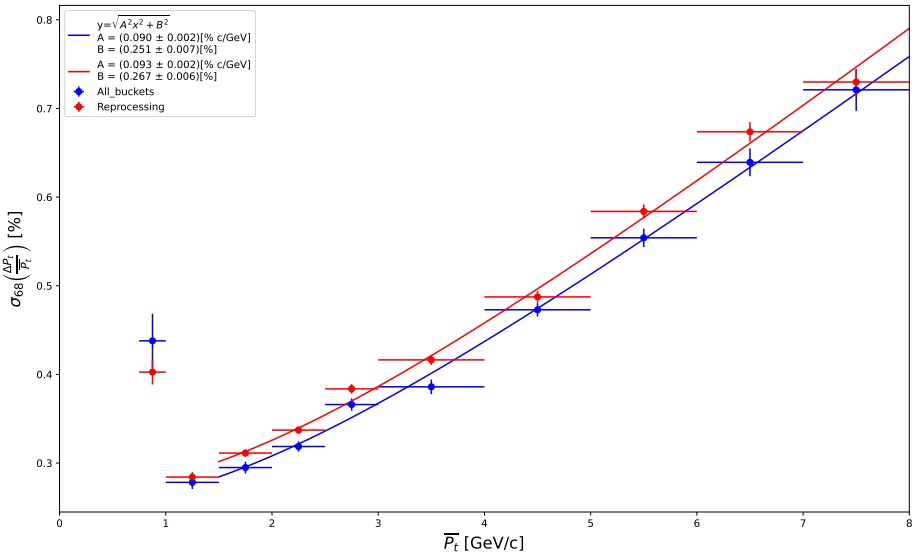

Figure 4.20: Relative P_t vs average

Table 4.3: Parameter a for final resolution fit

Helix parameter	All_buckets	Reprocessing
d_0 [μm]	9.89 ± 0.22	10.16 ± 0.27
z_0 [μm]	14.17 ± 0.27	14.65 ± 0.28
ϕ_0 [mrad]	0.11 ± 0.02	0.12 ± 0.02
$\tan\lambda$ [10^-3]	0.25 ± 0.01	0.25 ± 0.01

Table 4.4: Parameter b for final resolution fit

Helix parameter	All_buckets	Reprocessing
d_0 [μm GeV/c]	21.87 ± 0.72	21.81 ± 0.79
z_0 [μm GeV/c]	20.06 ± 0.78	19.22 ± 0.73
ϕ_0 [mrad GeV/c]	1.65 ± 0.03	1.64 ± 0.03
$\tan\lambda$ [10^-3 GeV/c]	1.54 ± 0.03	1.54 ± 0.03

The fit parameters for P_t resolution are for All_buckets:

$$A = 0.090 \pm 0.002 \text{ [\% c/GeV]}$$

$$B = 0.251 \pm 0.007 \text{ [\%]}$$

and for Reprocessing:

$$A = 0.093 \pm 0.002 \text{ [\% c/GeV]}$$

$$B = 0.267 \pm 0.006 \text{ [\%]}$$

And just like in Sect. 2.4 we will find the systematic errors caused by setting the range of the resolution plots by comparing the results with the same plots but for up to 15 GeV/c. These plots can be found in the appendix in Figs. A.16, A.17 and A.18. The resolutions are presented in Tables 4.5, 4.6 and below them for P_t.

Table 4.5: Parameter a with systematic error

Helix parameter	All_buckets
d_0 [μm]	$9.89 \pm 0.22 \pm 0.54$
z_0 [μm]	$14.17 \pm 0.27 \pm 0.04$
ϕ_0 [mrad]	$0.11 \pm 0.02 \pm 0.01$
$\tan\lambda$ [10^-3]	$0.25 \pm 0.01 \pm 0.01$

Table 4.6: Parameter b with systematic error

Helix parameter	All_buckets
d_0 [μm GeV/c]	$21.87 \pm 0.72 \pm 0.91$
z_0 [μm GeV/c]	$20.06 \pm 0.78 \pm 0.06$
ϕ_0 [mrad GeV/c]	$1.65 \pm 0.03 \pm 0.01$
$\tan\lambda$ [10^-3 GeV/c]	$1.54 \pm 0.03 \pm 0.01$

$$A = 0.090 \pm 0.002 \pm 0.004 \text{ [\% c/GeV]}$$

$$B = 0.251 \pm 0.007 \pm 0.010 \text{ [\%]}$$

Conclusion

In this thesis the resolution of the Belle II detector was determined using cosmic muons.

In the first part of the thesis the concept of Particle Physics was introduced and the Belle II experiment was described. The motivations of the Belle II experiment were briefly mentioned, then the parts of the Belle II detector were described. The term alignment was also explained.

The main part of this thesis are chapters 2, 3 and 4. In the chapter 2 the method of analyzing the data was introduced. It was first applied to data from Monte Carlo simulation. Using this ideal scenario we established what the results for real data are expected to look like.

In the chapter 3 the analysis method was applied to two different alignments of data from experiment 12 and the results compared with the Monte Carlo simulation. It was determined that the Reprocessing alignment is superior to Prompt alignment. The resolutions for both alignments were determined.

In the chapter 4 more recent data was analyzed. The data was from experiments 20 to 24. It was separated into five parts. These parts were compared and after no major differences were found they were combined to acquire a better sample size. This new combined data was then analyzed and compared to the previous results for the Reprocessing alignment. The resolutions were determined to be the same for both data. The resolutions for parameters d_0 and z_0 can be seen in Fig. 4.18

Additionally, a Python script capable of providing all the results present in this thesis was developed. This script can be found in the attachments.

Bibliography

[1] Wikipedia. standard model [online]. [cit. 17.7.2022]. URL `https://www.belle2.org/project/super_kekb_and_belle_ii`.

[2] A. J. Bevan, B. Golob, Th. Mannel, et al. The Physics of the B Factories. 2014. doi: 10.48550/ARXIV.1406.6311.

[3] E. Kou, P. Urquijo, W. Altmannshofer, et al. The Belle II Physics Book. *Progress of Theoretical and Experimental Physics*, 2019(12), dec 2019. doi: 10.1093/ptep/ptz106.

[4] T. Abe, I. Adachi, K. Adamczyk, et al. Belle II Technical Design Report. November 2010.

[5] Belle II. Super KEKB and Belle II [online]. [cit. 17.7.2022]. URL `https://www.belle2.org/project/super_kekb_and_belle_ii`.

[6] V. Bertacchi, T. Bilka, N. Braun, et al. Track Finding at Belle II. *Comput.Phys.Commun. 259 (2021) 107610*, March 2020. doi: 10.1016/j.cpc.2020.107610.

[7] T. Bilka. Belle II Alignment Performance for 2020ab Data. Belle II internal note PH-2021-04. 2021.

List of Figures

List of Tables

List of Abbreviations

CP Charge-Parity

LER Low Energy Ring

HER High Energy Ring

SM Standard Model

VXD Vertex Detector

PXD Pixel Detector

LHC Large Hadron Collider

DEPFET DEPleted Field Effect Transistor

SVD Silicon Vertex Detector

CDC Central Drift Chamber

PID Particle Identification System

TOP Time-of-propagation

ECL Electronic Calorimeter

KLM K_L^0 and Muon Detector

MC data from Monte Carlo simulation

Prompt measured data after basic alignment

Stage2 measured data after more advanced alignment

A. Attachments

A.1 Monte Carlo Data Analysis

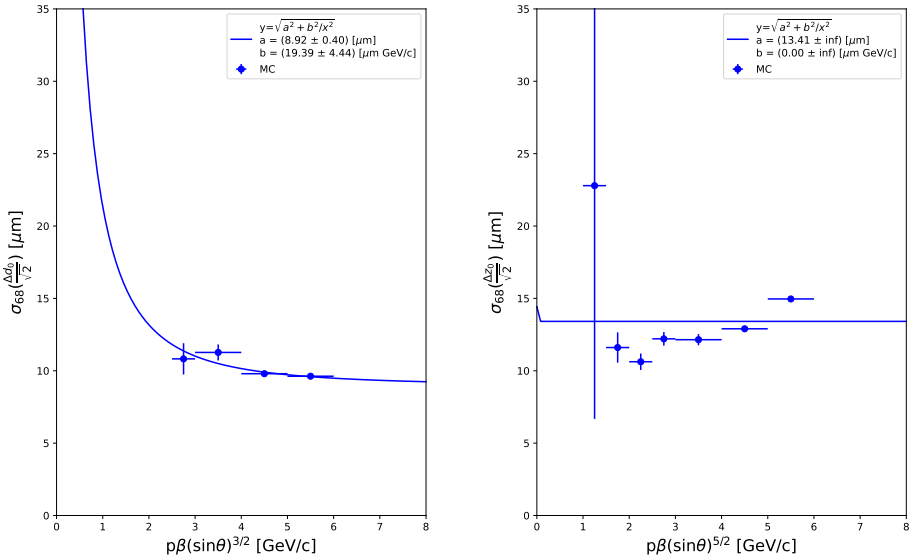

Figure A.1: Resolutions for d_0 (left) and z_0 (right) for 4 GeV/c $< P_t <$ 5 GeV/c

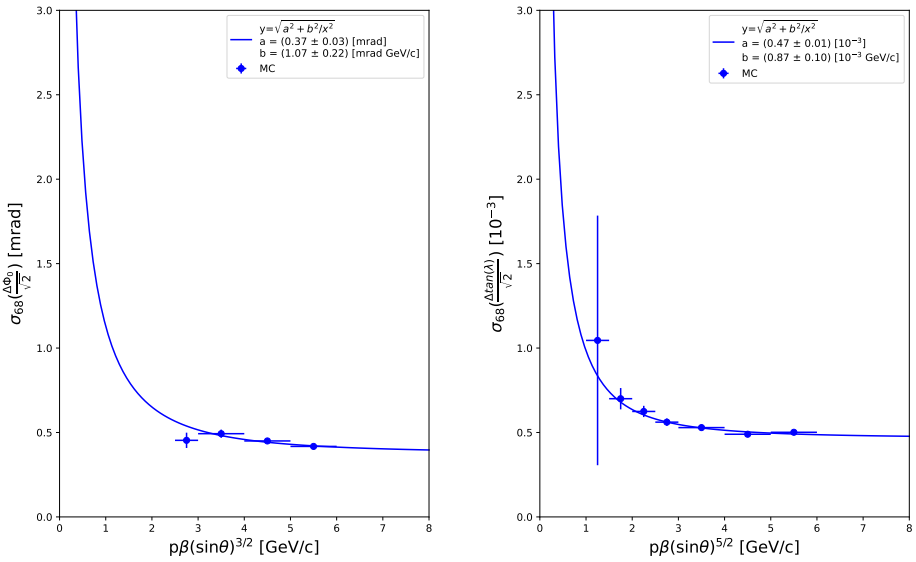

Figure A.2: Resolutions for ϕ_0 (left) and tan(λ) (right) for 4 GeV/c $< P_t <$ 5 GeV/c

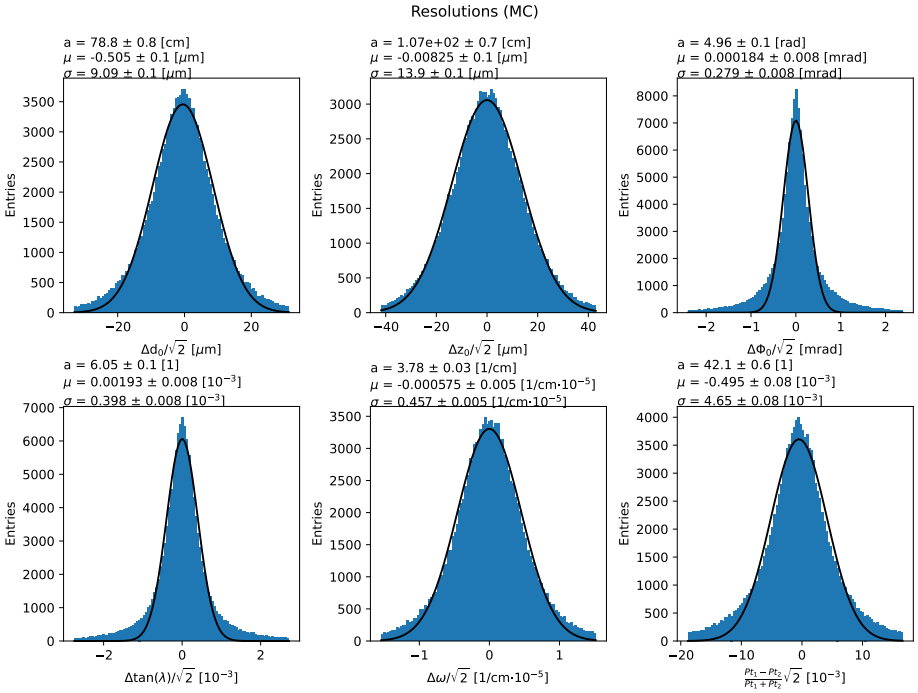

Figure A.3: Histograms of Δh for MC

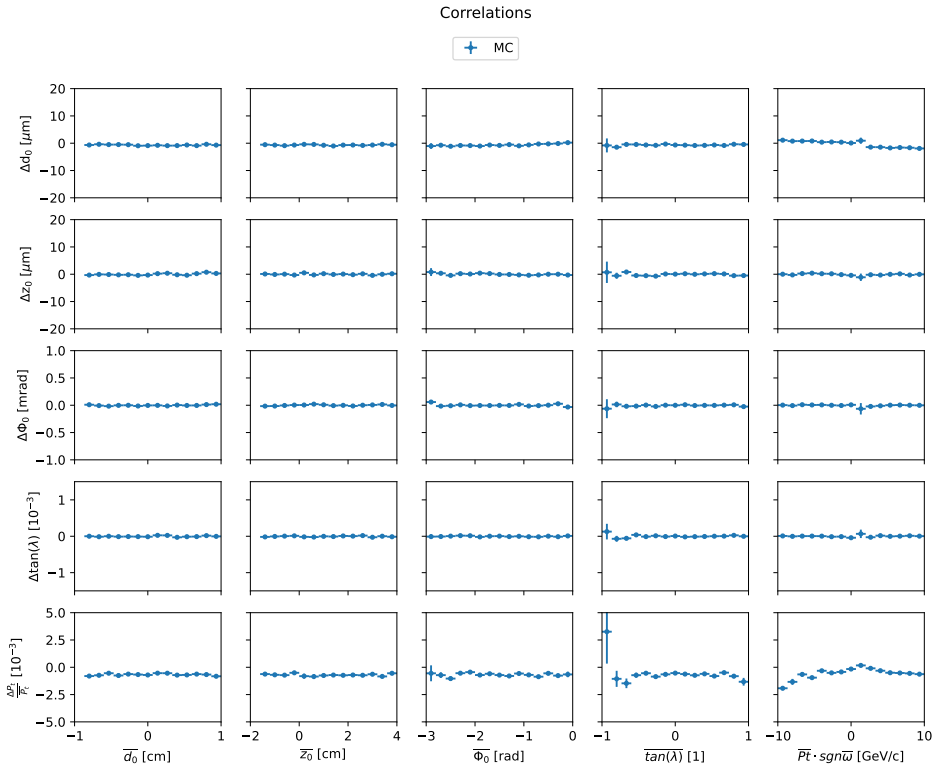

Figure A.4: Correlations of helix parameters for MC with P_t

A.2 Experiment 12 Data Analysis

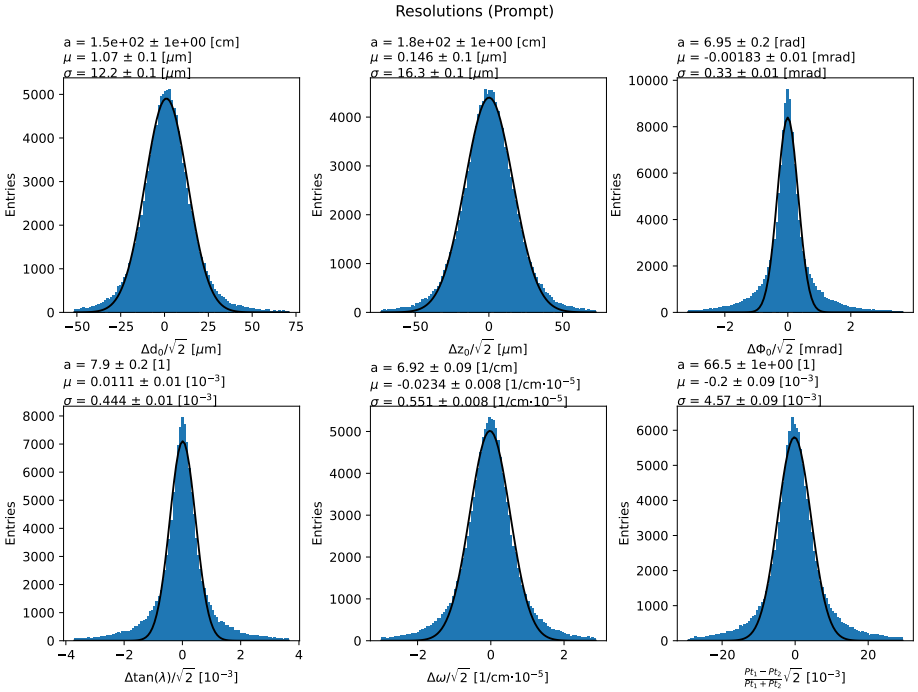

Figure A.5: Histograms of Δh for Prompt

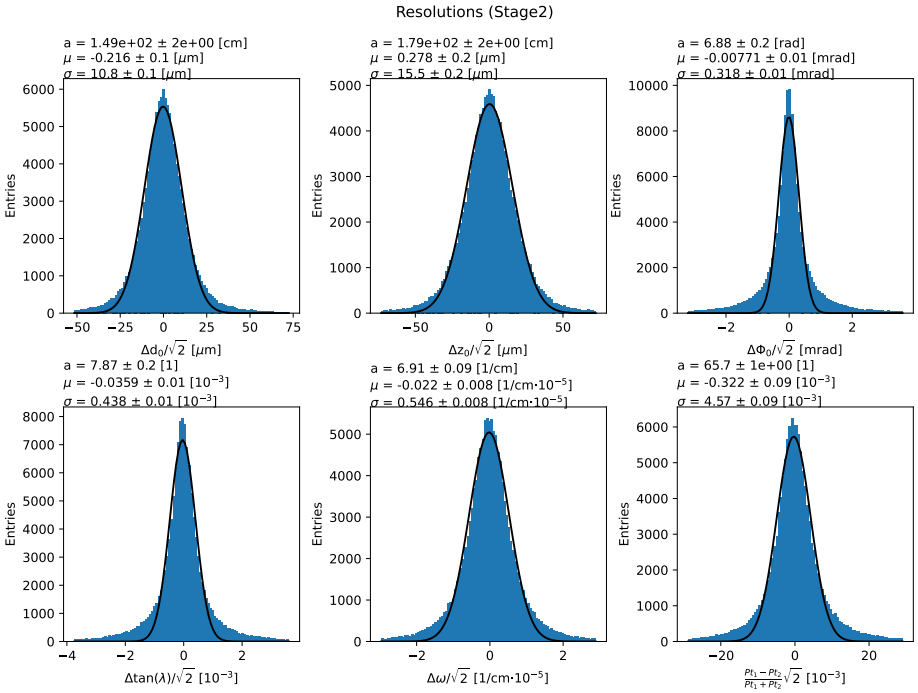

Figure A.6: Histograms of Δh for Stage2

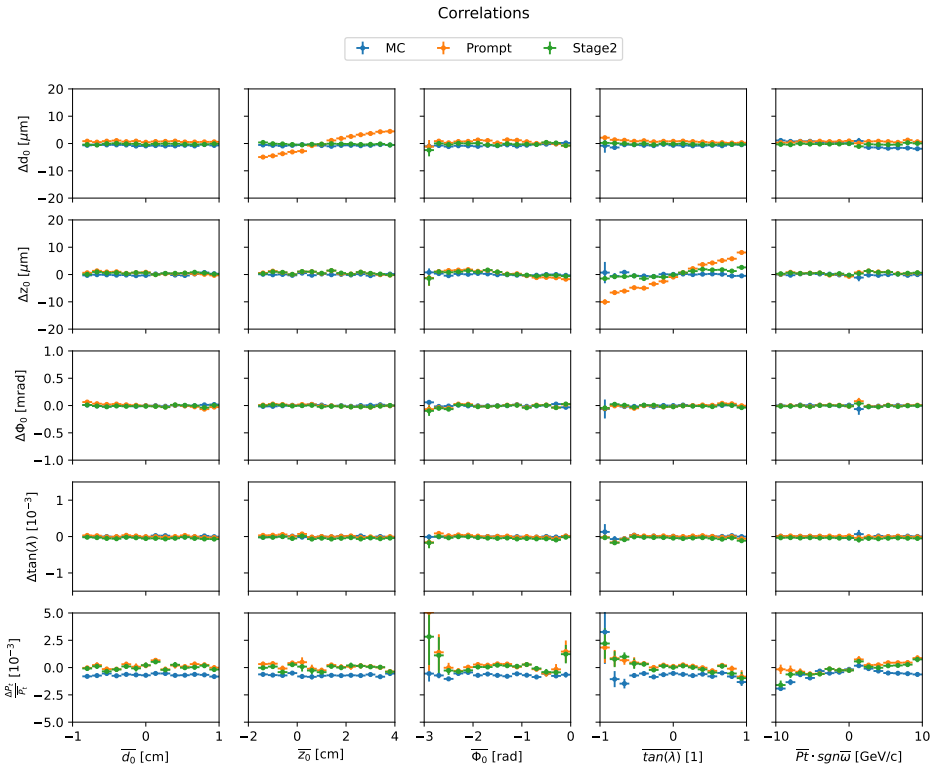

Figure A.7: Correlations of helix parameters with P_t

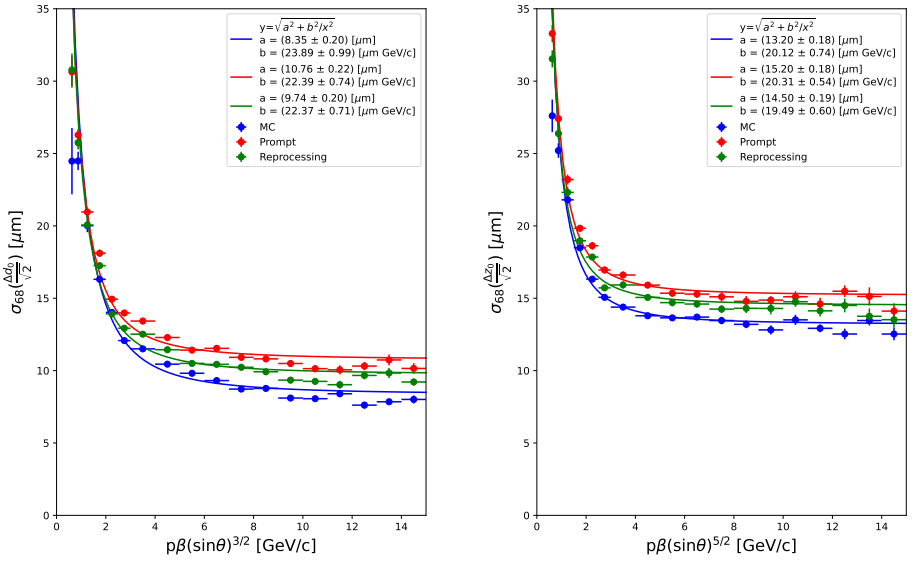

Figure A.8: Resolutions for d_0 (left) and z_0 (right)

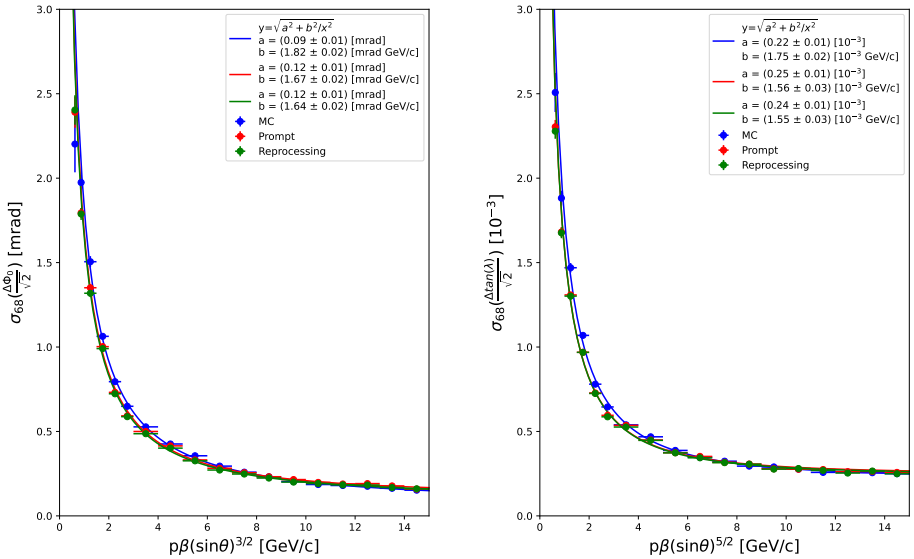

Figure A.9: Resolutions for ϕ_0 (left) and $\tan(\lambda)$ (right)

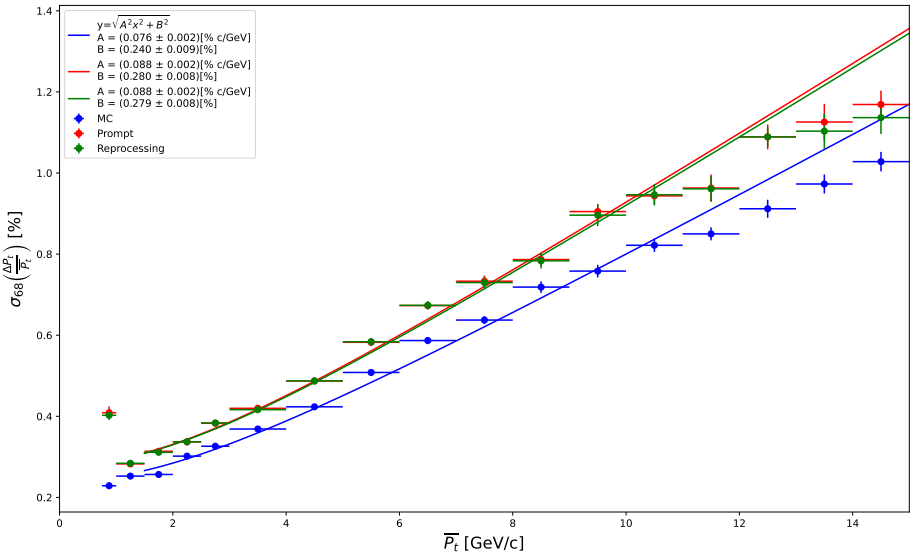

Figure A.10: Resolutions of relative P_t vs average P_t

A.3 Buckets 27 to 31 Analysis

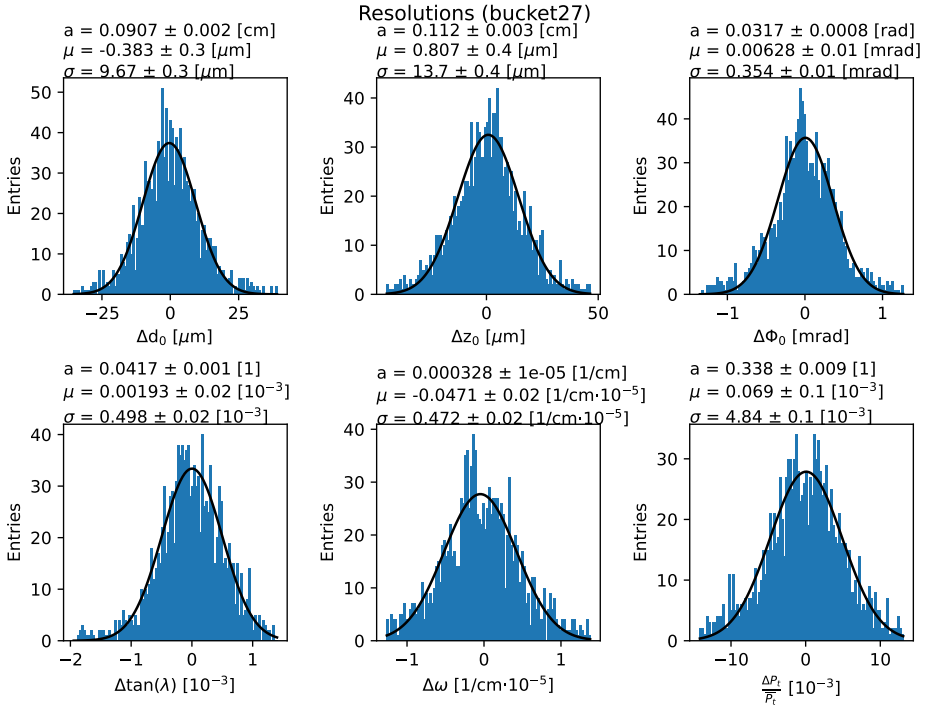

Figure A.11: Histograms of Δh for bucket27

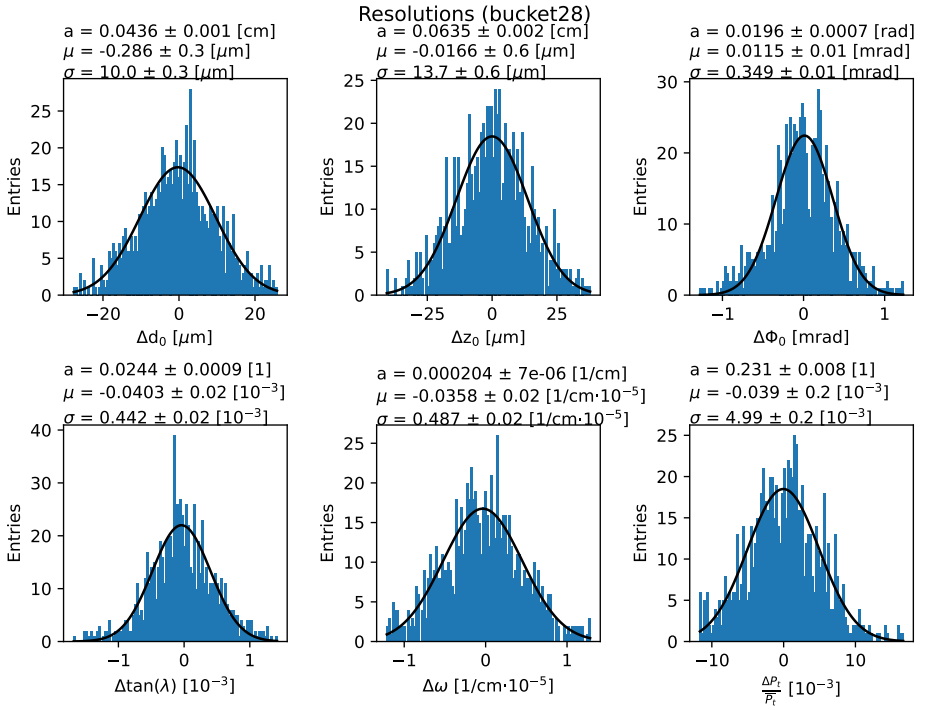

Figure A.12: Histograms of Δh for bucket28

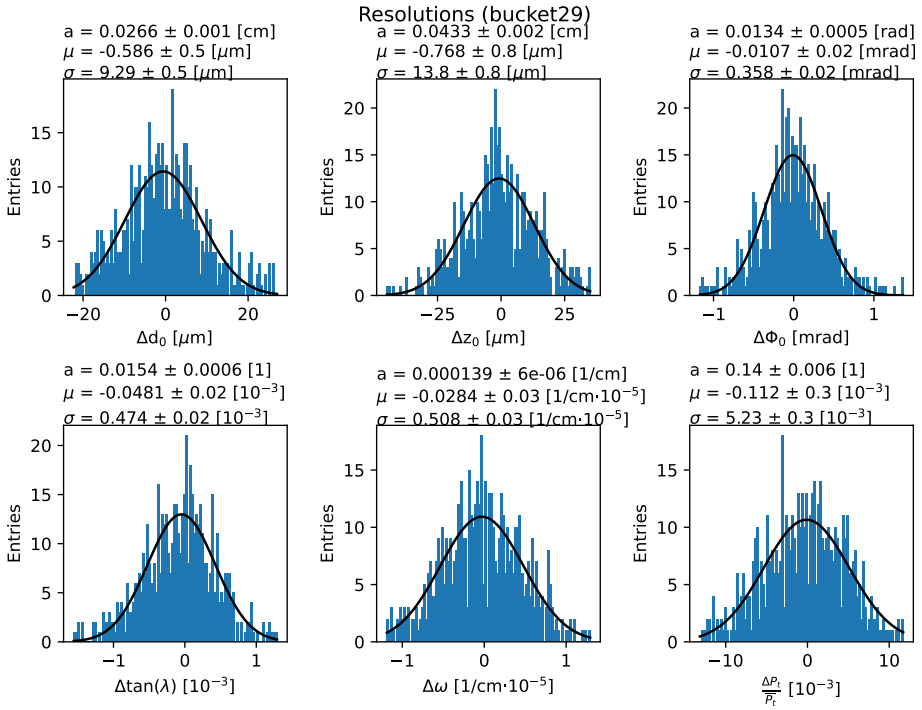

Figure A.13: Histograms of Δh for bucket29

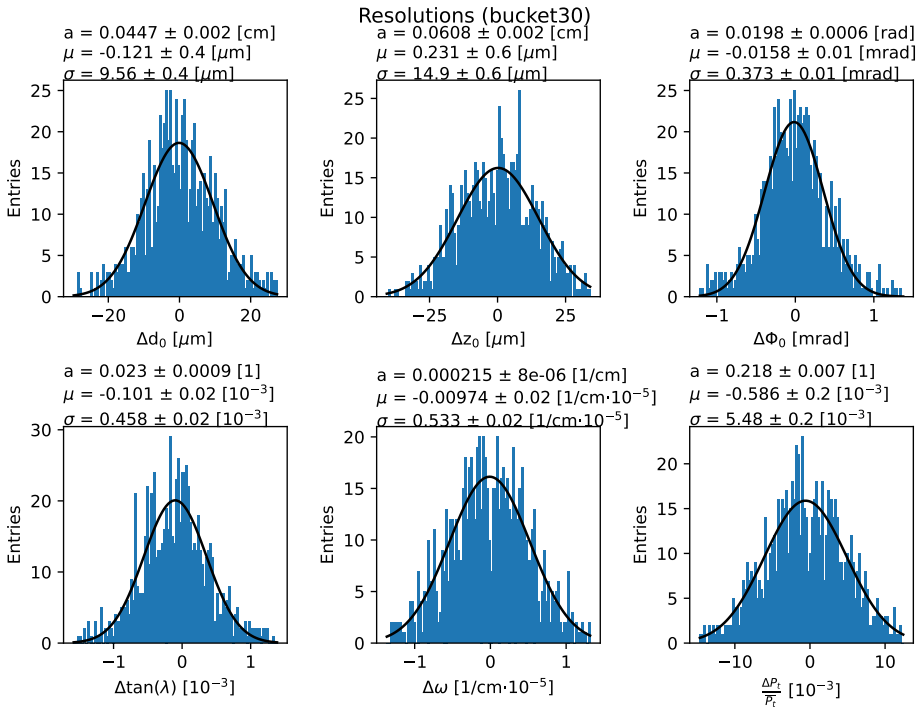

Figure A.14: Histograms of Δh for bucket30

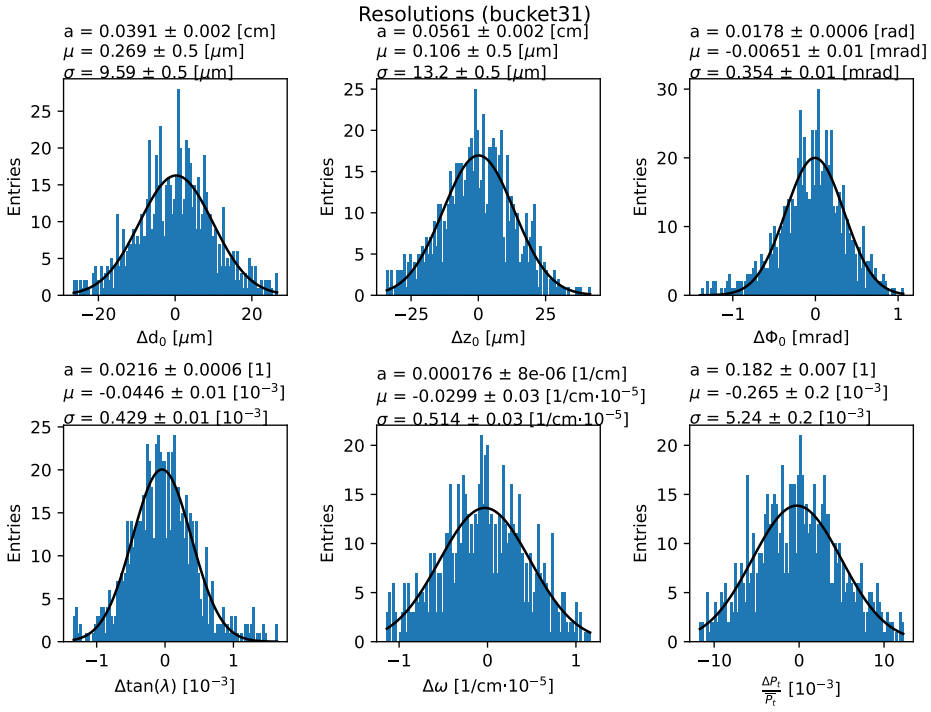

Figure A.15: Histograms of Δh for bucket31

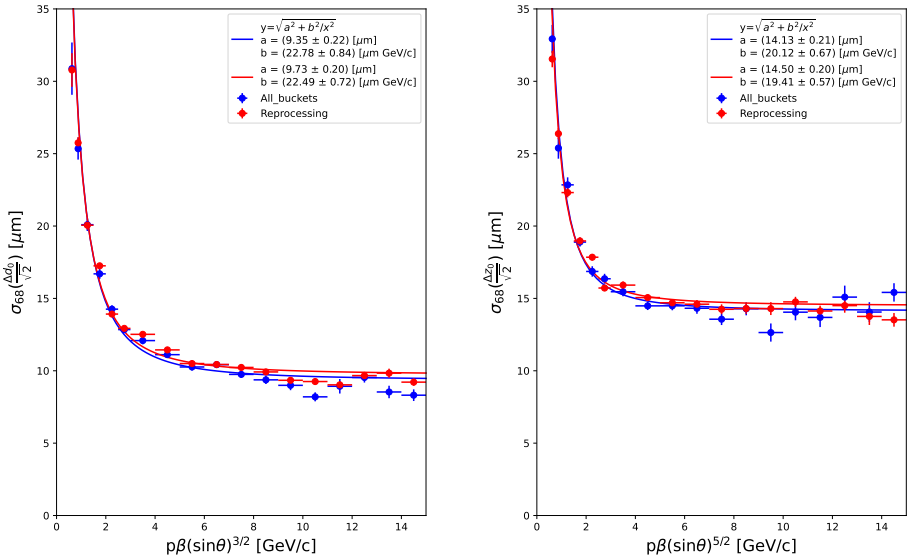

Figure A.16: Resolutions for d_0 (left) and z_0 (right)

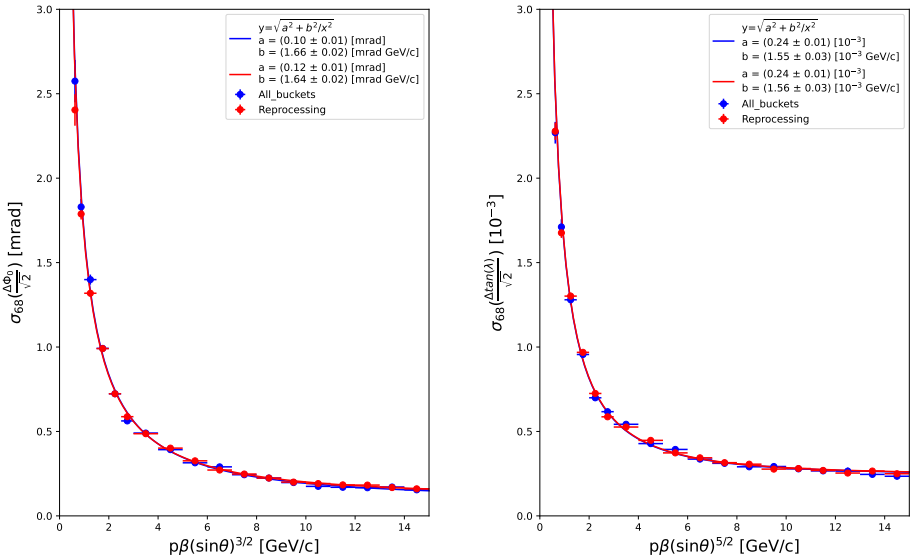

Figure A.17: Resolutions for ϕ_0 (left) and $\tan(\lambda)$ (right)

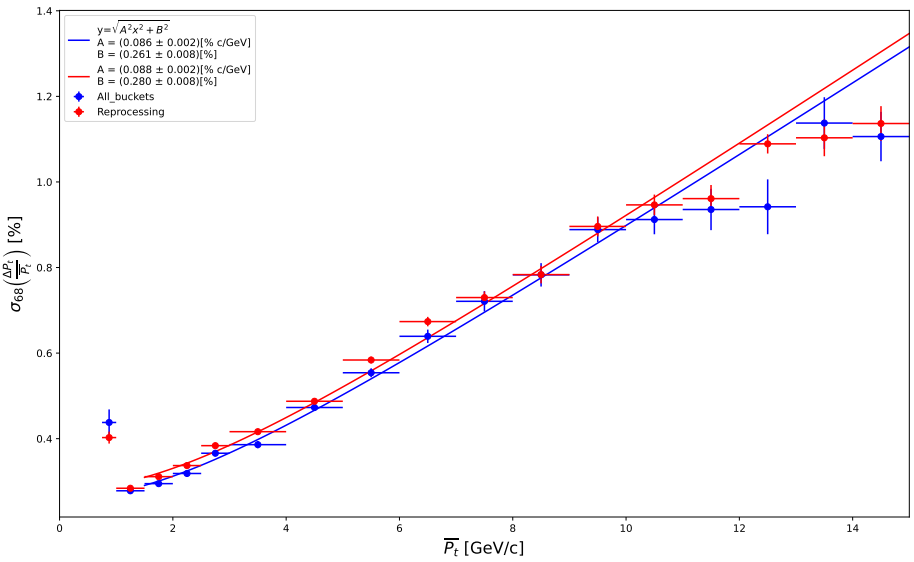

Figure A.18: Resolutions of relative P_t vs average P_t